Combining Multi-Satellite Remote and In-situ Sensing for Unmanned Underwater Vehicle State Estimation

Cesar A. Rojas[a,*], Paulo Padrão[a], Jose Fuentes[a], Gregory M. Reis[a], Arif R. Albayrak[b,c], Batuhan Osmanoglu[b] and Leonardo Bobadilla[a]

[a]Florida International University Knight Foundation School of Computing and Information Sciences, 11200 SW 8th Street, Miami, 33199, FL, USA
[b]NASA Goddard Space Flight Center, 8800 Greenbelt Rd, Greenbelt, 20771, MD, USA
[c]University of Maryland, Baltimore County, 1000 Hilltop Cir, Baltimore, 21250, MD, USA

ARTICLE INFO

Keywords:
remote sensing
machine learning
water quality estimation
state estimation
unmanned underwater vehicles

ABSTRACT

Accurate state estimation in underwater environments requires real-time, high-quality data on bathymetry and water quality due to the complexities of underwater terrains. Gathering this information reliably is a significant challenge. Our primary objective is to improve state estimation and precise positioning of underwater vehicles by incorporating 3D underwater maps generated using satellite-derived water quality estimators. We developed a comprehensive pipeline that collects in-situ data and supplements it with remote sensing images from Sentinel-2 (S2) and Landsat 8-9 (L8-9). Using supervised machine learning methods, we transformed the reflectance (R_{rs}) indices from these images, augmented with in-situ data, into water quality estimators. This enabled us to predict vital parameters like bathymetry, chlorophyll-a, dissolved oxygen, turbidity from S2 images, and sea surface temperature from L8-9 images. The generated underwater maps were introduced into an Extended Kalman Filter (EKF) for underwater vehicle state estimation, significantly enhancing its capabilities. The effectiveness of our EKF-based approach was validated through computer simulations. Additionally, we introduced a streamlined data management plan to expedite the creation of machine learning datasets and applications as a valuable secondary artifact. Our research primarily contributes to the enhanced state estimation of UUVs, with potential improvements in water quality monitoring and disaster response strategies.

1. Introduction

Robot state estimation in underwater environments pose significant challenges for various marine applications, including exploration, environmental monitoring, and disaster management. The complexities arise from the dynamic and often obscured nature of underwater settings, requiring access to real-time data on bathymetry and water quality metrics. Obtaining such data, especially in remote or hazardous areas, remains a persistent challenge.

The primary objective of this study is to enhance the state estimation capabilities of underwater robots by incorporating comprehensive 3D maps of underwater terrains, referred to as the Satellite-Derived Underwater Environment (SDUE). To achieve this, we developed a method to create these 3D maps by combining satellite-acquired and in-situ data. This approach enables underwater robots to detect and address harmful water events promptly (e.g., algal blooms, fish kills). In addition to our primary goal, we also introduce a streamlined data management plan to expedite the creation of machine learning datasets and applications, which serves as a valuable secondary artifact of our research.

Our methodology relies on remote sensing imagery from Sentinel-2 (S2) and Landsat 8-9 (L8-9) satellites (detailed in Appendices 5 and 6). Through supervised machine learning, we establish a relationship between remote sensing reflectance (R_{rs}) indices from these satellite images and key water quality indicators such as chlorophyll-a, dissolved oxygen (DO), turbidity, and temperature. Notably, we incorporate sea surface temperature (SST) estimation from L8-9 imagery, adding a nuanced understanding of the thermal aspects of underwater environments.

*Corresponding author
croja022@fiu.edu (C.A. Rojas); plope113@fiu.edu (P. Padrão); jfuen099@fiu.edu (J. Fuentes); gregory@cs.fiu.edu (G.M. Reis); rustem.a.albayrak@nasa.gov (A.R. Albayrak); batuhan.osmanoglu@nasa.gov (B. Osmanoglu); bobadilla@cs.fiu.edu (L. Bobadilla)
ORCID(s): 0000-0002-2964-3574 (C.A. Rojas); 0000-0003-3966-0279 (P. Padrão); 0000-0002-6477-5820 (J. Fuentes); 0000-0002-5734-2699 (G.M. Reis); 0000-0003-2097-2432 (L. Bobadilla)

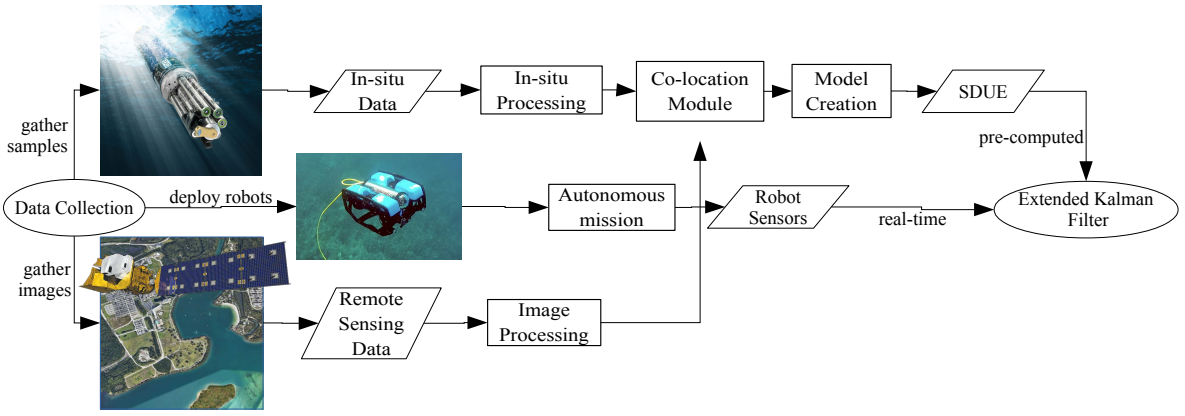

Figure 1: A diagram illustrating our approach to satellite-supported robot State Estimation.

The SDUE map, combining temperature estimates from L8-9 with other water quality estimates from S2, provides a comprehensive representation of the underwater environment. It offers insights into spatio-temporal temperature variability and its interaction with other water quality parameters. Additionally, we implement a robust data management plan to facilitate the acquisition, organization, and storage of diverse datasets essential for developing and training our machine learning estimators. This map is then introduced as an additional sensor in an Extended Kalman Filter (EKF) configured for underwater state estimation.

This article presents the following key contributions:

- Proposition of a machine learning application to make 3D satellite-derived underwater maps.
- Combines remote sensing with in-situ sensing to create water quality estimators.
- Utilization of an EKF to fuse map and robot sensors for enhanced state estimation.
- Introduction of a data management plan for acquisition and storage of datasets.
- Proves the system's practicality in real-world Biscayne Bay, Florida application.

While earlier versions of our methodology were featured in Rojas, Padrao, Fuentes, Albayrak, Osmanoglu and Bobadilla (2022a) and Rojas, Reis, Albayrak, Osmanoglu, Bobadilla and Smith (2022b), this article delves deeper, emphasizing the expansion of the SDUE map and thoroughly validating our EKF based state estimation strategy.

1.1. Study Limitations

Our methodology leverages the EKF to optimize underwater robot state estimation by integrating data from the SDUE, GPS, and other sensors (see Figure 1). The modular nature of our approach, represented in Figure 1, incorporates methods chosen for their simplicity and demonstrated effectiveness in previous studies. It is essential to note that our selected methods may not be universally optimal for all marine environments and should be assessed case by case. Our case study primarily serves to validate the overall workflow, recognizing that while using an EKF in an underwater setting is not novel, our pipeline is a significant contribution. Please note that while the ultimate goal is for all tasks to be fully automated, particularly the construction and usage of the SDUE, in this study, the SDUE will be precomputed, preloaded, and used as is. Our future work discusses potential improvements in this regard.

2. Related Work

Recent studies have extensively explored the application of statistical methods and machine learning algorithms to both in-situ and remote sensing data. Various investigations have been conducted to assess the effectiveness of

individual data sources and their fusion. Works by Gholizadeh, Melesse and Reddi (2016), Nazeer, Bilal, Alsahli, Shahzad and Waqas (2017), Hafeez, Wong, Ho, Nazeer, Nichol, Abbas, Tang, Lee and Pun (2019), and Cruz, Costa, Vinga, Krippahl and Lopes (2021) demonstrate the potential of these techniques, often presenting performance metrics such as cross-validation accuracy scores and root-mean-square error (RMSE). Our focus is on machine learning methods that combine both sources of data to enhance environmental mapping accuracy and precision. Specifically, we emphasize supervised learning methods where in-situ data is used to train models that analyze remote sensing data. In this context, "labeling" refers to the process of assigning ground truth values from in-situ data to corresponding remote sensing observations for training purposes. We will present remote sensing indices that will be labeled.

2.1. Scientific Data Management

Effective data management is crucial for the reproducibility, reliability, and overall usability of project data in data-intensive fields. Our project adopts data management strategies outlined in Documentation (2017) and Hook, Santhana Vannan, Beaty, Cook and Wilson (2010). These strategies emphasize a bifurcated approach, separating data management and metadata creation.

Data management includes organizing file hierarchies, implementing file retention protocols, and adhering to data formatting standards. These practices ensure structured, accessible, and long-lasting data storage. Simultaneously, metadata creation involves generating descriptive files with comprehensive information, enhancing data interpretability and traceability, covering process steps, instrumentation details, timestamps, geographic locations, and more.

To enhance data handling efficiency, we follow a file naming convention inspired by Osmanoglu (2020). This convention facilitates quick and accurate identification of our data assets. Collectively, these practices contribute to establishing a robust and effective data management system, underpinning the success and impact of our work.

2.2. Satellite-Derived Bathymetry

In the field of bathymetry, Caballero and Stumpf (2019) demonstrated a significant contribution by deriving bathymetry from S2 images. Focusing on South Florida, their method involved calculating pseudo-satellite-derived bathymetry (pSDB) and labeling it using data points extracted by nautical charts. The final step involved the application of a linear regression estimator. The pSDB calculations are represented as follows:

$$pSDB_{S2} = \frac{\log(1000\pi B3)}{\log(1000\pi B2)}, \quad pSDB_{S2a} = \frac{\log(1000\pi R_{rs}(560))}{\log(1000\pi R_{rs}(492))} \tag{1}$$

In a follow-up study, Caballero, Stumpf and Meredith (2019) investigated the influence of water quality parameters, such as turbidity and chlorophyll-a, on the maximum predicted water column depth, enhancing the evaluation of pSDB.

2.3. Satellite-Derived Chlorophyll-a

Remote sensing plays a crucial role in estimating chlorophyll-a in water bodies. Mishra and Mishra (2012) introduced the Normalized Difference Chlorophyll Index (NDCI), designed for chlorophyll-a concentration estimation in estuaries and coastal turbid waters. The NDCI calculations are expressed as:

$$NDCI_{S2} = \frac{B5 - B4}{B5 + B4}, \quad NDCI_{S2a} = \frac{R_{rs}(704) - R_{rs}(665)}{R_{rs}(704) + R_{rs}(665)} \tag{2}$$

Building on this, Caballero, Fernández, Escalante, Mamán and Navarro (2020) demonstrated the use of S2 images and NDCI to detect algal blooms in coastal waters. However, they emphasized the significance of in-situ data in identifying harmful algal blooms caused by toxic algae species.

2.4. Satellite-Derived Turbidity

The introduction of the Normalized Difference Turbidity Index (NDTI) by Lacaux, Tourre, Vignolles, Ndione and Lafaye (2007) enables remote estimation of turbidity. This index has been effectively employed by Tomchenko, Khyzhniak, Kravtsova and Singh (2022) for estimating turbidity from S2 imagery. The NDTI calculations are represented as:

$$NDTI_{S2} = \frac{B4 - B3}{B4 + B3}, \quad NDTI_{S2a} = \frac{R_{rs}(665) - R_{rs}(560)}{R_{rs}(665) + R_{rs}(560)} \tag{3}$$

2.5. Satellite-Derived Dissolved Oxygen

In studying the effectiveness of spectral predictors for DO, Salas, Kumaran, Partee, Willis and Mitchell (2022) focused on the Sentinel Water Mask (SWM). This remote sensing index, originally designed for open water detection in S2 images, proved to be one of the more effective predictors for DO. SWM can be calculated as:

$$SWM_{S2} = \frac{B2 + B3}{B8 + B11}, \quad SWM_{S2a} = \frac{R_{rs}(492) + R_{rs}(560)}{R_{rs}(833) + R_{rs}(1614)} \tag{4}$$

2.6. Satellite-Derived Sea Surface Temperature

L8-9's thermal infrared sensor (TIRS) bands ST10 and ST11 can estimate SST by calibrating with referenced data. SST has been estimated using a regression-based approach, such as the Split-Window (SW) algorithm Fu, Chen, Guo, Chu and Zheng (2020); Bayat and Hasanlou (2016). There are several SW algorithms, and one commonly used version is the multichannel sea surface temperature (MSST) algorithm:

$$SST = a + bT_{10} + c(T_{10} - T_{11}) \tag{5}$$

Here, T_{10} and T_{11} represent the brightness temperatures measured by ST10 and ST11, respectively. The coefficients a, b, and c are empirical coefficients derived from a calibration process. In some cases, the calibration involves selecting reference pixels from the TIRS image that have known SST values from in-situ measurements and then establishing an empirical relationship between TIRS radiance values and SST. The precision of the resulting SST values relies on both the quality of the reference data and the coefficients obtained from the calibration process.

2.7. Satellite-Assisted Robot State Estimation

A cutting-edge application of remote sensing and in-situ data involves unmanned vehicles for planetary exploration. Kodgule, Candela and Wettergreen (2019) devised a method that integrates these data types within a Markov Decision Process framework. At its core, the technique involves spectral unmixing of lower-resolution satellite data using higher-resolution in-situ data collected as the robot visits points of interests. This approach significantly enhances the robot's understanding of its environment, improving the decision-making process during exploration.

2.8. Underwater State Estimation

The underwater environment poses distinct challenges for state estimation, particularly due to the absence of GPS signals. As highlighted by Paull, Saeedi, Seto and Li (2014), achieving precise state estimation remains a significant hurdle in this context. Prediction errors in position, often resulting from process and sensor noise, can significantly impact the success of unmanned underwater operations Manzanilla, Reyes, Garcia, Mercado and Lozano (2019). To tackle these challenges, state estimation filters, including the EKF Potokar, Norman and Mangelson (2021), the Unscented Kalman Filter (UKF) Allotta, Caiti, Costanzi, Fanelli, Fenucci, Meli and Ridolfi (2016), and particle filter (PF) Fox et al. (2001) have emerged as widely adopted methods for precise underwater state estimation. These filters fuse information from primary sensors such as inertial measurement units (IMUs) and Doppler velocity logs (DVLs) to minimize state estimation errors. Terrain-augmented methods, incorporating environmental data, are employed to build maps aiding state estimation in GPS-limited scenarios. For example, Salavasidis, Munafò, McPhail, Harris, Fenucci, Pebody, Rogers and Phillips (2021) explores using bathymetry measurements to enhance IMU-based state estimation in arctic continental environments. Similarly, our approach integrates water quality measurements to build maps within the same paradigm. Due to its simplicity and convenience, we use an EKF strategy to handle non-linearities in vehicle motion and observation models, providing a robust solution for underwater state estimation.

3. Problem Formulation

3.1. Satellite-Derived Underwater Environment

We define our ocean work environment (OWE) as a 3D space denoted by $\mathcal{W} \subset \mathbb{R}^3$. This space is divided into 2D water layers at varying depths, represented by L. The overall workspace $\mathcal{W}$ is expressed as the union of these 2D water layers:

$$\mathcal{W} = w_1 \cup w_2 \cup \cdots \cup w_L \tag{6}$$

Each layer $l \in \{1, \ldots, L\}$ is modeled as a 2D space $w_l \subset \mathbb{R}^2$ and discretized into a 2D grid. The freely accessible water space at each layer is denoted as:

$$E_l = w_l \setminus O_l \tag{7}$$

Here, $O_l \subset \mathbb{R}^2$ denotes an inaccessible region for the underwater vehicle. Thus, the free workspace is defined across the entire $\mathcal{W}$ as:

$$\mathcal{E} = E_1 \cup E_2 \cup \cdots \cup E_L \tag{8}$$

We denote $\mathcal{C}$ as the collection of all 2D cells within a bounding convex polygon $\mathcal{P}$, where $\mathcal{P} \subseteq w_1$ symbolizes our area of interest (AOI). Each cell has a center characterized by WGS84 coordinates, (x, y, l), representing longitude, latitude, and water depth. The resolution of the remote sensing data is covered by equally sized grid tiles with each unit of l corresponding to a depth of 1 meter.

We define $\mathcal{Q} = (d, b, i, m)$ as a satellite query configuration, where d is a satellite identifier and b, i, m are lists of requested R_{rs} bandwidths, indices, and metadata, respectively. Remote sensing data is represented as $\rho : \mathcal{C} \times \mathcal{Q} \times T_1 \rightarrow \mathbb{R}^k$, where $T_1 = [0, t_1)$ is the data collection time interval, and $k = |b| + |i| + |m|$ is the total number of variables.

We denote $\beta : T_2 \rightarrow \mathbb{R}^n$ as the collection of all available in-situ data, where $T_2 = [0, t_2)$ represents the collection time interval and n is the number of in-situ sensors. In-situ data collected on the surface by Unmanned Surface Vehicles (USVs) is denoted as β_u, where $\beta_u \subseteq \beta$.

Let $\mathcal{S} : \mathcal{W} \rightarrow \mathbb{R}^j$ be a Satellite-Derived Underwater Environment (SDUE), computed through a supervised machine learning estimator. This computation involves the mapping, or labeling, of ρ with β_u. The shared values exhibit identical coordinates and demonstrate a negligible difference in collection time. The parameter j denotes the number of predicted water parameters, with the values labeled in ρ exhibiting a strong correlation with the in-situ data. Within the 3D SDUE, the estimation of in-situ measurements is positioned at the center of each cell, covering a $10x10$-meter area from a layer situated within $\mathcal{P}$.

Problem 1: *Given an OWE $\mathcal{W}$ of interest, a bounding convex polygon $\mathcal{P}$, a satellite configuration $\mathcal{Q}$, a collection of remote sensing data ρ, and a collection of in-situ data β, the task is to compute an SDUE $\mathcal{S}$.*

3.2. Vehicle Model

Consider an Unmanned Underwater Vehicle (UUV) denoted as $\mathcal{A}$ acting as an agent, located at the starting point $\mathbf{x}_0 = (x_0, y_0, 0) \in \mathcal{W}$. $\mathcal{A}$ collects in-situ data represented as β_a, where $\beta_a \subseteq \beta_u$. It possesses the capability to traverse the freely accessible water space $\mathcal{E}$ and move across different layers within the OWE.

$\mathcal{A}$ is modeled as a discretized, non-linear system, where the motion model of the vehicle is defined as $f(\mathbf{x}_k, \mathbf{u}_k) + \mathbf{q}_k$. Here, $\mathbf{x}_k$ represents the state vector, and $\mathbf{u}_k$ denotes the input control vector. The relationship between the current state and the next state is given by $\mathbf{x}_{k+1} = f(\mathbf{x}_k, \mathbf{u}_k) + \mathbf{q}_k$, with $\mathbf{x}_0$ being the initial position of the vehicle. The observation model of the vehicle is denoted as $h(\mathbf{x}_k) + \mathbf{r}_k$, where $\mathbf{q}_k$ and $\mathbf{r}_k$ account for additive, zero-mean noise to accommodate model and sensing imperfections at each iteration k.

Assuming $\mathcal{A}$ to have a rigid body and considering its movement to be slow and at a constant speed v, we neglect its dynamics for safety reasons. Additionally, we assume the water current is irrotational and possesses only horizontal linear velocity components. The sensors on $\mathcal{A}$ include GPS, IMU (gyros, accelerometers), a depth sensor, and water quality sensors.

Mathematically characterizing $\mathcal{A}$, we represent it as a discretized, non-linear system:

$$\begin{aligned} \mathbf{x}_{k+1} &= f(\mathbf{x}_k, \mathbf{u}_k) + \mathbf{q}_k \\ \mathbf{z}_k &= h(\mathbf{x_k}) + \mathbf{r}_k \end{aligned} \tag{9}$$

where $f(\mathbf{x}_k, \mathbf{u}_k)$ is the motion model, $h(\mathbf{x_k})$ is the observation model, and $\mathbf{z}_k$ is the observation obtained by $\mathcal{A}$ at step k. The stochastic processes $\{\mathbf{q}_k\}_{k\in\mathbb{N}}$ and $\{\mathbf{r}_k\}_{k\in\mathbb{N}}$ are characterized by multivariate uncorrelated random variables, with $\mathbf{q}_k \sim \mathcal{N}(\mathbf{0}, \mathbf{Q}_k)$ and $\mathbf{r}_k \sim \mathcal{N}(\mathbf{0}, \mathbf{R}_k)$.

3.3. Extended Kalman Filter Framework

The EKF algorithm comprises two primary phases: prediction and update. Figure 2 illustrates the steps involved to enhance understanding of these phases. Let $\mathcal{X}$ and $\mathcal{Z}$ denote the state and observation planes, respectively. The state plane serves as the domain where the state $\mathbf{x}_k$ evolves over time; however, it is not directly accessible or observable. Conversely, the measurement plane is accessible, representing the domain where the measurements resulting from the state are observed. To predict the system state using the EKF filter, the initial estimate $\mathbf{x}_0$ and covariance $\mathbf{P}_0$ are needed. Additionally, the noise covariance $\mathbf{Q}_k$ and state transition model are required. The process starts with initializing the vehicle on the surface using GPS data. The covariance matrix $\mathbf{P}_0$ is set considering sensor-related uncertainties. The EKF necessitates computing the Jacobian of the state transition function $\mathbf{F}_k$ and the observation model $\mathbf{H}_k$. The EKF procedure for state estimation is detailed in Algorithm 1. We then formulate the following problem

Problem 2: *Given an OWE $\mathcal{W}$, an SDUE $\mathcal{S}$, and the desired trajectory τ, compute an estimated trajectory $\hat{\tau}$ minimizing tracking error.*

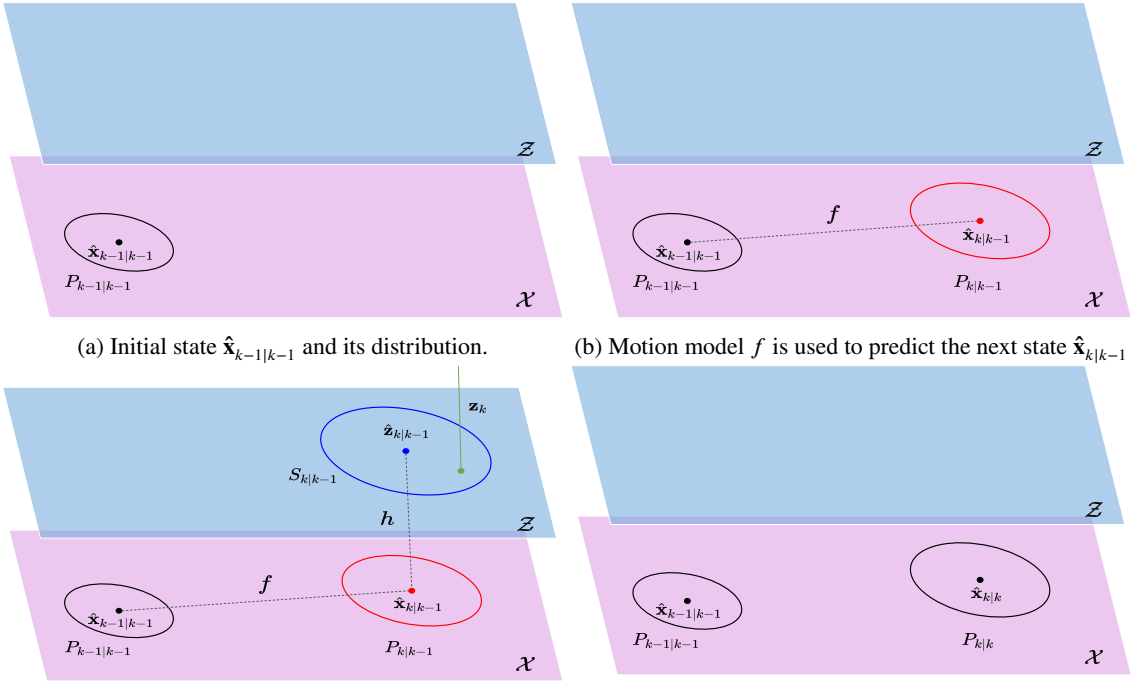

(a) Initial state $\hat{\mathbf{x}}_{k-1|k-1}$ and its distribution.

(b) Motion model f is used to predict the next state $\hat{\mathbf{x}}_{k|k-1}$

(c) The observation model h is used to project the predicted state $\hat{\mathbf{x}}_{k|k-1}$ from the state plane into the observation plane.

(d) The predicted state is updated based on the observed measurement and observation model, and the resulting state is the posterior $\hat{\mathbf{x}}_{k|k}$.

Figure 2: Explanation of the EKF algorithm.

Algorithm 1 EKF($\hat{\mathbf{x}}_{k-1|k-1}, \mathbf{P}_{k-1|k-1}, \mathbf{z}_k$)

Input: $\hat{\mathbf{x}}_{k-1|k-1}$: current state estimate, $\mathbf{P}_{k-1|k-1}$: covariance matrix, $\mathbf{z}_k$: current measurement vector
Initialization: $\hat{\mathbf{x}}_{0|k} \in \mathbb{R}^d$, $\mathbf{P}_{0|k} \in \mathbb{R}^{d\times d}$

$\hat{\mathbf{x}}_{\mathbf{k}|\mathbf{k-1}} = f(\hat{\mathbf{x}}_{k-1|k-1}, \mathbf{u}_{k-1|k-1}) + \mathbf{q}_{k-1|k-1}$ ▷ Prediction
$\mathbf{F}_k = \frac{\partial f}{\partial \mathbf{x}}\Big|_{\hat{\mathbf{x}}_{k-1|k-1}}$
$\mathbf{P}_{k|k-1} = \mathbf{F}_k \mathbf{P}_{k-1|k-1} \mathbf{F}_k^\top + \mathbf{Q}_k$
$\mathbf{H}_k = \frac{\partial h}{\partial \mathbf{x}}\Big|_{\hat{\mathbf{x}}_{k|k-1}}$ ▷ Update
$\mathbf{K}_k = \mathbf{P}_{k|k-1}\mathbf{H}_k^\top \left(\mathbf{H}_k \mathbf{P}_{k|k-1} \mathbf{H}_k^\top + \mathbf{R}_k\right)^{-1}$
$\hat{\mathbf{x}}_{k|k} = \hat{\mathbf{x}}_{k|k-1} + \mathbf{K}_k(\mathbf{z}_k - h_k(\hat{\mathbf{x}}_{k|k}))$
$\mathbf{P}_{k|k} = \left(\mathbf{I} - \mathbf{K}_k \mathbf{H}_k\right)\mathbf{P}_{k|k-1}$
return $\hat{\mathbf{x}}_{k|k}, \mathbf{P}_{k|k}$

4. Methods

The methodology involves two key components: dataset creation and trajectory estimation. The initial phase consists of data collection, data processing, and organizing data for reproducibility. This encompasses all aspects of dataset creation. Subsequently, the second part utilizes the generated SDUE to enhance the state estimation capabilities of an underwater vehicle.

4.1. Data Plan

A machine learning research project involves stages: data collection, processing, colocation, and application development. For reproducibility, we present a comprehensive data plan and organized file hierarchy. The root structure has "projects" and "events". Teams maintain projects, each with relevant datasets. Significant events (e.g., Fish Kill, Algal Bloom) are documented with metadata files, views, or other relevant files. Metadata files in a view can reference datasets across projects, providing visualizations (e.g., statistics, charts). Throughout the stages of the research project, the data plan comprises the following actions: machine learning dataset creation, data organization, metadata documentation, and automation. Details of these actions will be given in the upcoming sections.

4.1.1. Machine Learning Dataset Creation

We utilize methodologies established in prior projects to create machine learning datasets, adhering to our comprehensive data plan. This process involves bulk downloading remote sensing images from sources such as Sentinel-2 (S2) and Landsat 8-9 (L8-9) and consolidating in-situ data from previous missions. The data is processed first to produce a higher quality dataset, then to produce a colocated dataset. After colocation with in-situ data, the resulting dataset is used in machine learning applications. Metadata files are generated for each stage of the data lifecycle: raw, processed, colocated, and application-ready. To provide contextual understanding, related documents, research papers, news articles, and media are included in the project files.

4.1.2. Data Organization

For improved accessibility, we use a hierarchy and consistent naming with a simple file system. Consider a Content Management System (CMS) for complex projects needing governance, access controls, or metadata management.

Data Hierarchy: Group data hierarchically by projects, events, and categories. Datasets follow a four-level "Data Processing" structure Earth Science Data Systems (2016). Begin at level 0 post-acquisition, advance to level 1 after metadata creation, level 2 with additional processing, and level 3 after colocation of remote sensing and in-situ data. Level 4 datasets are created with machine learning-based estimators. Categorize datasets within levels, e.g., isolated or time series, using CMS tags. Consider sublevels like "Level 2a" Earth Science Data Systems (2016).

Distinct views of these datasets can be created by saving them with different file extensions. Maintain consistent filenames across views, only appending or altering extensions. Avoid unnecessary duplication. We primarily use Comma Separated Values (CSV).

File Naming: We adopt a detailed convention including project name, cardinal direction, date, time, mission number, description, version, file number, and extension (see table 2). As data progresses through the different levels,

Table 1
Data set file hierarchy

- Projects
  - Project_1 (named using conventions)
    - Media (Images, video, audio)
    - Data
      - Level_1 (Unprocessed)
        - Remote_sensing
          - Landsat_8
          - Sentinel_2
        - In-situ
          - Time_series
          - Isolated
      - Level_2 (Processed)
      - Level_3 (Colocated Data)
      - Level_4 (Applications)
        - Application_1.json
    - Documents (Proposal, abstracts, etc. . .)
    - Literature (Related Work)
    - Articles (News Websites, PSAs, etc. . .)
    - Vehicles (Robots, drones, boats, etc. . .)
    - Instruments (Sensors on vehicles)
    - Source (Relevant source code)
      - Bulk_Downloader_1.py
      - Processor_1.py
      - Colocation_1.py
      - Model_1.py
      - View_1.py
    - Locations (Geo json files)
  - Project_1.json (Metadata as json files)
- Events (Fish kill, algal bloom, etc. . .)
  - Event_1.json (References to relevant data in projects close to the date of event)

Example Project: Biscayne_Bay_Coastal_2018_to_present-FIU

these naming conventions can be adjusted for convenience. These are primarily meant for in-situ data gathered by the project team, as naming conventions for remote sensing data are already well established.

4.1.3. Metadata Documentation

Publicly available software with graphical user interfaces (GUIs) or command-line interfaces (CLIs) can be used for bulk data download and processing. These tools often generate metadata files. To avoid redundancy, reuse existing metadata. For example, if a CSV file includes metadata in its first row, there is no need for duplication. Similarly, when an atmospheric correction processor creates multiple metadata files, referencing them is more efficient than duplicating information. Geospatial details are stored in GeoJSON files, these files should be noted. Essential details, like manual process steps, should be included in the metadata file to streamline documentation.

Table 2
Data file naming conventions

• Project Name (Abbreviated) • Site Cardinal Direction (e.g., N, NW, E, SE) • Date (YYYYMMDD) and Time (Time is Optional) • Mission Number (###) • Data Description • Version • File Number (For data split across multiple files) • Extension
Example Data File: BB2018FIU_N_20220127_001_Water_Quality_V01_F01.csv

Metadata files should provide thorough information on data, including column data, source details, acquisition and access dates, process steps, and references to key personnel, instruments, and vehicles. Include any other pertinent information related to the research project. Appendix Table 7 outlines recommended metadata fields.

4.1.4. Automating the Process

We develop custom CLI software that automate tasks typically performed through a GUI. Stored in the source folder, these automation scripts handle data collection and processing tasks, improving reproducibility and efficiency. These scripts provide detailed, programmatically executed steps for bulk data download, processing corrections, colocation, estimator creation, estimation, and generating additional views. The metadata file references the automation script used for dataset creation, ensuring reproducibility, accessibility, and ease of use for future projects.

4.2. Data Collection Missions

We represent our OWE using a bounding convex polygon, serving as the basis for all remote sensing data requests (Figure 3a). The OWE encompasses all AOIs. A smaller bounding convex polygon is set as $\mathcal{P}$ to be our AOI (Figure 4a).

We deploy a manned vessel with an EXO2, a Multiparameter sonde product offered by YSI, submerged in the water for in-situ data collection, β_u, serving as ground truth for labeling remote sensing data, ρ. Water depth measurements from nautical chart 11467, a dataset created and published by the National Oceanic and Atmospheric Administration (NOAA), complement β_u. This chart is treated as in-situ data and utilized similarly to methods described in Caballero et al. (2019). Figures 5a, 5b, and 5c illustrate the manned vessel, in-situ data collection sites, and NOAA chart 11467, respectively.

Subsequently, we configure a satellite to request an S2 image and an L8-9 image captured on the day closest to the in-situ data collection date. This request includes all available bands and metadata information over $\mathcal{W}$, with the additional condition of minimal cloud contamination. In this instance, we downloaded both an L8-9 image and an S2 image captured on October

4.3. Data Processing

Bathymetry measurements from NOAA chart 11467 are georeferenced using GPS coordinates and compiled into a CSV file. The L8-9 and S2 images undergo ACOLITE atmospheric correction, with sun glint correction enabled. The corrected image is processed in the ESA Sentinel Application Platform (SNAP) to extract pixels corresponding to in-situ data locations.

We filter out non-water pixels, such as land and vessels. For L8-9 images, the Landsat Quality Assurance band is used, while for S2 images, a simple threshold method on band 8 (NIR) is employed. Another approach for water pixel filtering is suggested by Drakopoulou, Kapsimalis, Parcharidis and Pavlopoulos (2018), and optimal threshold selection is discussed by Kavats, Khramov, Sergieieva, Puputti, Joutsenvaara and Kotavaara (2022).

NDCI, pSDB, NDTI, and SWM are calculated, labeled with in-situ data for chlorophyll-a, bathymetry, turbidity, and DO. ST10 and ST11 from L8-9 are incorporated into temperature calculations. Surface in-situ data is co-located

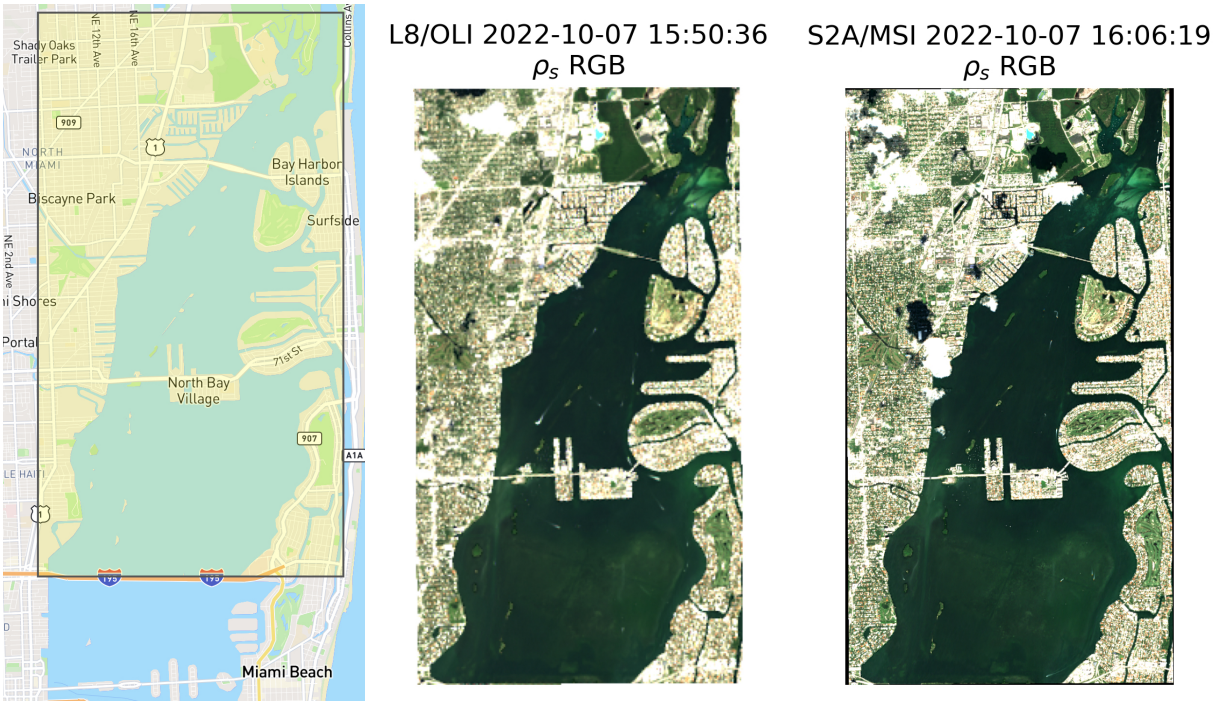

(a) (b) (c)

Figure 3: Ocean work environment (OWE). (a) OWE represented as a bounding convex polygon. (b) L8-9 image of the OWE, atmospherically corrected via ACOLITE. (c) S2 image of the OWE, atmospherically corrected via ACOLITE.

with remote sensing data using the SNAP Pixel extraction tool, training linear regression estimators predicting surface chlorophyll-a, bathymetry, turbidity, dissolved oxygen, and temperature.

Underwater in-situ data, labeled with water depth measurements, is used to create georeferenced K-nearest neighbors (KNN) regressors predicting changes in surface estimates for deeper water depths. The surface estimate for each pixel is extended to lower levels using the KNN regressor. Pixels contaminated by land are filtered out.

S2 10m resolution reduces outlier effects by ensuring each pixel is co-located with multiple in-situ measurements. Negative estimates are replaced with predetermined positive in-situ measurements. Another satellite query is created for the latest S2 image over $\mathcal{W}$, corrected with ACOLITE. For each pixel, calculated NDCI, pSDB, NDTI, and SWM serve as inputs for estimators predicting surface chlorophyll-a, bathymetry, turbidity, and DO. A similar request is made for an L8-9 image, with ST10 and ST11 bands used for estimating SST.

To create SDUE and address *problem 1*, we estimate surface values for each water quality parameter and use georeferenced KNN regressors to predict lower levels. These estimators collectively predict chlorophyll-a, bathymetry, turbidity, DO, and temperature up to the maximum predicted depth.

4.4. Trajectory estimation using EKF

Now, we present our approach that aims to use the available SDUE in our domain of interest $\mathcal{W}$.

4.4.1. Motion Model

We assume the underwater vehicle can be modeled as a rigid body moving slowly at a constant speed v. Let $\mathcal{X}$ denote the state space encompassing all possible states, and $\mathcal{U}$ represent the action space comprising all possible actions. The mission's completion time is denoted as T, and we divide the interval $[0, T]$ into segments of size Δt. We define t_k as $k\Delta t$, referring to the time or instant k as $\mathbf{v}_k$ for any vector or matrix $\mathbf{v}$ at time t_k. Consequently, at any given instant k, the vehicle can be described by the following expression:

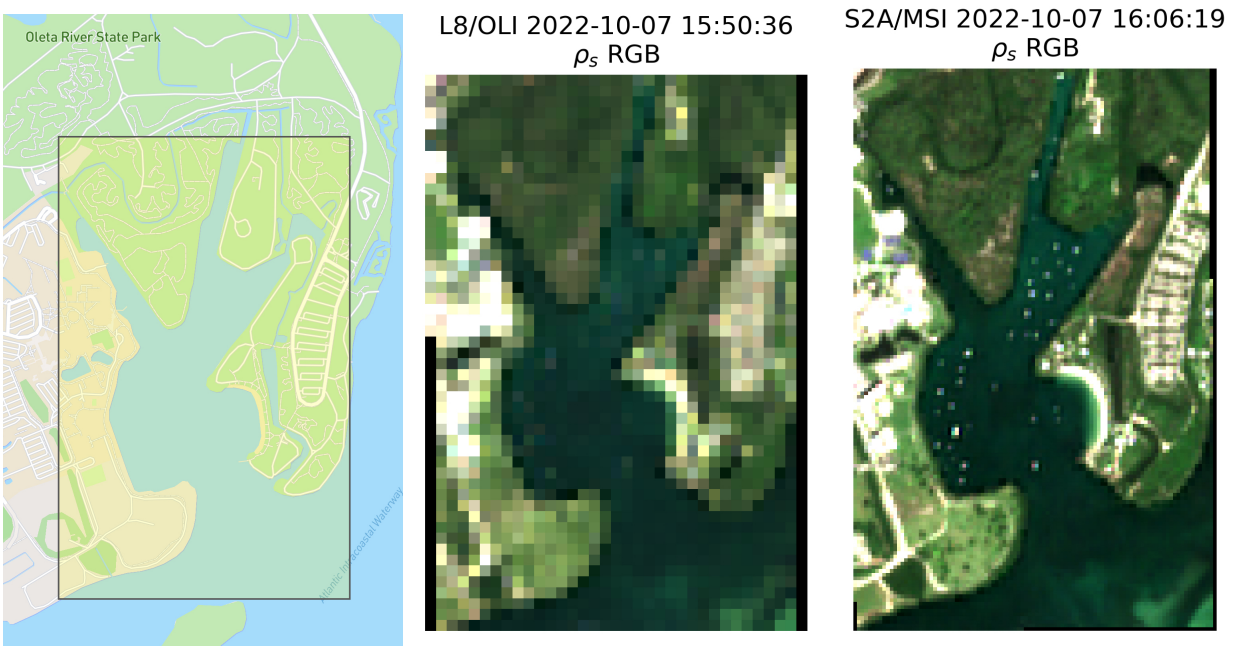

(a) (b) (c)

Figure 4: Remote sensing data retrieval. (a) AOI represented as a bounding convex polygon within the OWE. (b) RGB bands of an L8-9 image of the AOI, atmospherically corrected via ACOLITE. (c) RGB bands of an S2 image of the AOI, atmospherically corrected via ACOLITE.

$$\begin{aligned}\mathbf{x}_k &= (x^{(k)}, y^{(k)}, l^{(k)}, \psi^{(k)}, v^{(k)})^\top \in \mathcal{X} \\ \mathbf{u}_k &= (v^{(k)}, u_l^{(k)}, \omega^{(k)})^\top \in \mathcal{U}\end{aligned} \tag{10}$$

where (x, y) is the underwater horizontal position of the vehicle, l is the depth, ψ is the vehicle's heading, v is the vehicle's translational velocity, and ω is the angular velocity. Considering that u_l is an action that directly affects a change in depth ($\dot{l} = u_l$), the simplified kinematic model of the vehicle is defined as:

$$\mathbf{x}_{k+1} = \mathbf{A}\mathbf{x}_k + \mathbf{B}_k\mathbf{u}_k + \mathbf{q}_k \tag{11}$$

where the state transition matrix $\mathbf{A}$ and the input matrix $\mathbf{B}$ are given by

$$\mathbf{A} = \begin{bmatrix} 1 & 0 & 0 & 0 & 0 \\ 0 & 1 & 0 & 0 & 0 \\ 0 & 0 & 1 & 0 & 0 \\ 0 & 0 & 0 & 1 & 0 \\ 0 & 0 & 0 & 0 & 0 \end{bmatrix}, \quad \mathbf{B} = \begin{bmatrix} \Delta t \cos(\psi^{(k)}) & 0 & 0 \\ \Delta t \sin(\psi^{(k)}) & 0 & 0 \\ 0 & \Delta t & 0 \\ 0 & 0 & \Delta t \\ 1 & 0 & 0 \end{bmatrix} \tag{12}$$

and $\mathbf{q}_k$ is zero-mean noise distributed as $\mathbf{q}_k \sim \mathcal{N}(\mathbf{0}, \mathbf{Q}_k)$ with covariance given by

$$\mathbf{Q}_k = \begin{bmatrix} 1^2 & 0 & 0 & 0 & 0 \\ 0 & 1^2 & 0 & 0 & 0 \\ 0 & 0 & 1^2 & 0 & 0 \\ 0 & 0 & 0 & \left(\frac{\pi}{360}\right)^2 & 0 \\ 0 & 0 & 0 & 0 & 1^2 \end{bmatrix} \tag{13}$$

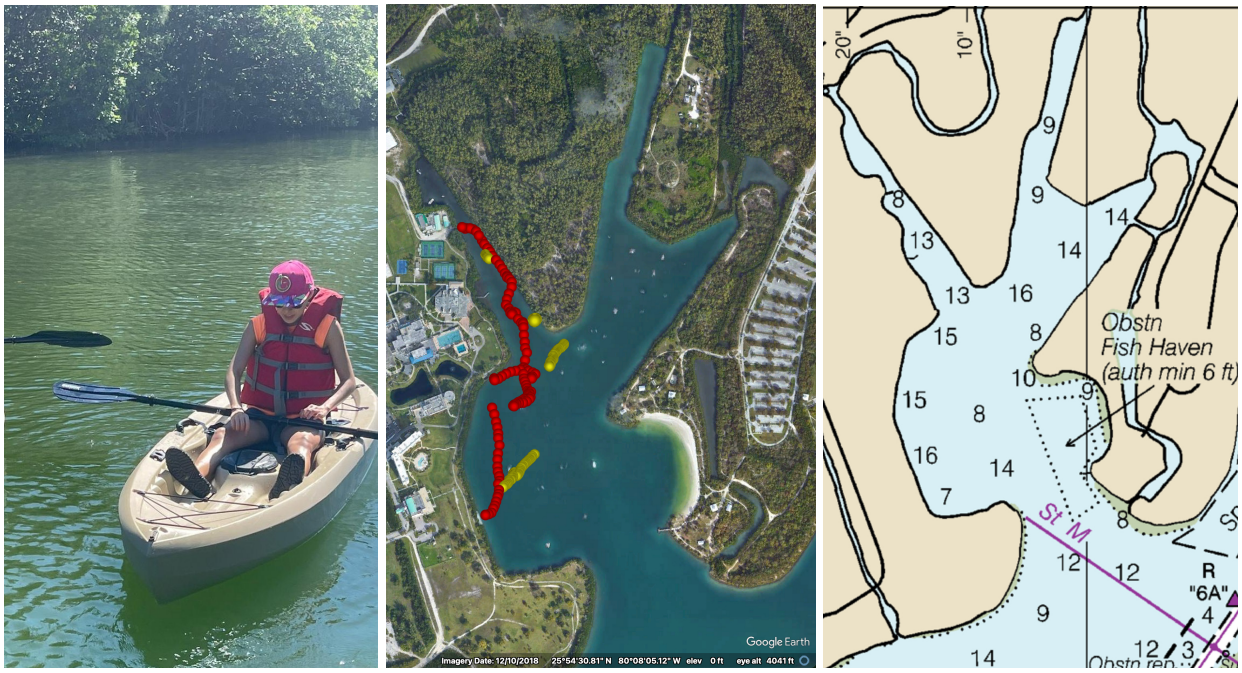

(a) (b) (c)

Figure 5: Data collection mission. (a) Manned vessel deployed to the AOI preparing for a data collection mission. (b) Locations where in-situ data were collected. Red dots represent surface measurements, and yellow dots represent underwater measurements. (c) Portion of NOAA chart 11467 showing water depths (in feet) in our AOI.

4.4.2. Observation Model

The UUV is equipped with a set of sensors, including GPS, IMU (gyros, accelerometers), and water quality sensors (DO, chlorophyll-a, temperature, and turbidity sensors). Observations of the vehicle's state are affected by uncertainties arising from sensor imperfections and the dynamic underwater environment. The observation space, denoted as $\mathcal{Z}$, encompasses all potential sensor observations $\mathbf{z}_k \in \mathcal{Z}$ at iteration k. The observation model $h(\mathbf{x}_k)$, assuming the availability of GPS sensor readings at the surface, is represented as:

$$\mathbf{z}_k = h(\mathbf{x}_k) = \begin{bmatrix} 1 & 0 & 0 & 0 & 0 \\ 0 & 1 & 0 & 0 & 0 \\ 0 & 0 & 1 & 0 & 0 \end{bmatrix} \mathbf{x}_k + \mathbf{r}_k \tag{14}$$

where $\mathbf{r}_k$ is zero-mean noise distributed as $\mathbf{r}_k \sim \mathcal{N}(\mathbf{0}, \mathbf{R}_k)$ with covariance given by:

$$\mathbf{R}_k = \begin{cases} \mathbf{R} & \text{if } -0.30 \leq l^{(k)} \leq 0 \\ \mathbf{R}(\mathbf{x}_k) & \text{if } l^{(k)} \leq -0.30, \end{cases} \quad \text{with } \mathbf{R} = \begin{bmatrix} 1^2 & 0 & 0 \\ 0 & 1^2 & 0 \\ 0 & 0 & 1^2 \end{bmatrix}, \; \mathbf{R}(\mathbf{x}_k) = (1 - 0.1l^{(k)}) \begin{bmatrix} 1^2 & 0 & 0 \\ 0 & 1^2 & 0 \\ 0 & 0 & 1^2 \end{bmatrix}. \tag{15}$$

Moreover, due to the uncertainty associated with the 3D SDUE map construction, $\mathbf{R}_k$ is designed to consider the uncertainty as the UUV dives, i.e., the deeper the vehicle descends, the higher the uncertainty is. When the UUV is underwater, GPS measurements are unavailable; as a result, calculating $\mathbf{z}_k = h(\mathbf{x}_k)$ (14) using GPS sensors is not feasible. To address this challenge, a unique aspect of this work involves employing the SDUE to map chlorophyll-a, dissolved oxygen, temperature, and turbidity measurements for estimating locations, leveraging available water feature sensor data from observational measurements. The SDUE is precomputed and supplied to the UUV before deployment.

We extend the function $h(\mathbf{x}_k)$ to be computed underwater, providing water feature measurements at location $\mathbf{x}_k$ for the SDUE $\mathcal{S}(\mathbf{x})$. At iteration k, local sensor probes installed in the UUV are utilized to measure chlorophyll-a,

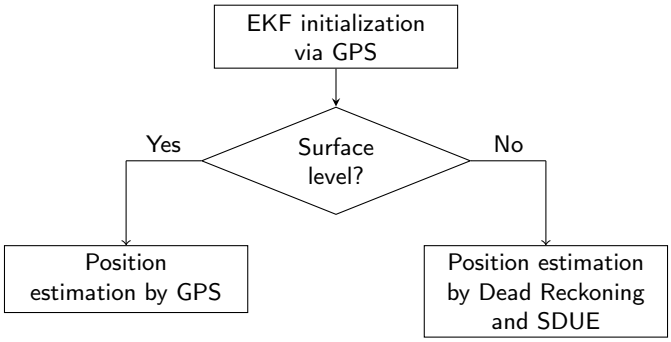

Figure 6: Observation function behavior for the EKF Framework

dissolved oxygen, temperature, and turbidity as $\mathbf{m}_k \in \mathbb{R}^4$. The UUV uses the SDUE $\mathcal{S}(\mathbf{x})$ to determine a location $\mathbf{z}_k$ as described in (16), implicitly defining the observation function $h(\mathbf{x}_k) = \mathbf{z}_k$. However, the SDUE might provide multiple $\mathbf{z}_k$ possible locations with similar water feature measurements (solving $\mathcal{S}(\mathbf{x}_k) = \mathbf{z}_k$ for $\mathbf{x}_k$), potentially resulting in inaccurate estimations if these locations are sufficiently distant.

To address this issue, we constrain (regularize) the optimization problem (16) by adding the restriction $(\mathbf{x} - \mathbf{x}_{k-1})^\top \mathbf{M}^{-1}(\mathbf{x} - \mathbf{x}_{k-1}) \leq 1$ to provide a reasonable candidate and enforce certain continuity between two subsequent iterations $\mathbf{x}_{k-1}$ and $\mathbf{x}_k$.

$$\begin{aligned} \mathbf{z}_k = h(\mathbf{x}_k) = \underset{\mathbf{x}\in\mathcal{W}}{\arg\min} \quad & ||\mathcal{S}(\mathbf{x}) - \mathbf{m}_k||_2^2 \\ \text{s.t.} \quad & (\mathbf{x} - \mathbf{x}_{k-1})^\top \mathbf{M}^{-1}(\mathbf{x} - \mathbf{x}_{k-1}) \leq 1. \end{aligned} \tag{16}$$

The matrix $\mathbf{M}$, a positive definite matrix treated as diagonal, restricts to possible value using a Mahalanobis distance. This constraint ensures a search for locations in the SDUE map with measurements close to the noisy ones collected by the agent $\mathbf{m}_k$. Equation (16) filters suitable state candidates $\mathbf{z}_k$, selecting points close to the previous estimation within an uncertainty ellipsoid centered at $\mathbf{x}_{k-1}$. This process typically yields a small number or a single unique candidate. However, it is important to note that, given a general SDUE, guaranteeing a unique solution may require excessive constraint in equation (16).

Regarding the theoretical aspects of the function h, it is reasonable to assume its differentiability based on the implicit function theorem and the nature of the implied functions in equation (16). Although, its Jacobian was calculated using a finite difference scheme to estimate each partial derivative.

The behavior of the solution obtained in (16) is detailed in Fuentes, Bobadilla and Smith (2022). In this scenario, $\mathbf{m}_k = \mathcal{S}(\mathbf{x}_k) + \varepsilon$, where $\varepsilon \sim \mathcal{N}(0, \Sigma)$ represents the noisy measurement collected at step k and state $\mathbf{x}_k$. Under these conditions, Fuentes et al. (2022) has shown constants m, K, and a function c such that

$$m||\varepsilon||_\infty \leq ||\mathbf{x}_k - \mathbf{z}_k||_2 \leq c(\varepsilon) \approx K||\varepsilon||_2. \tag{17}$$

When the vehicle is underwater, the state undergoes updates via dead-reckoning and estimations provided by the EKF for its position, assuming the existence of an SDUE map. The initial system state is defined as $\mathbf{x}_0 = (x^0, y^0, l^0, \psi^0, v^0)^\top$, and the covariance is initialized as $\mathbf{P}_0 = \mathbf{I}_{5\times5}$.

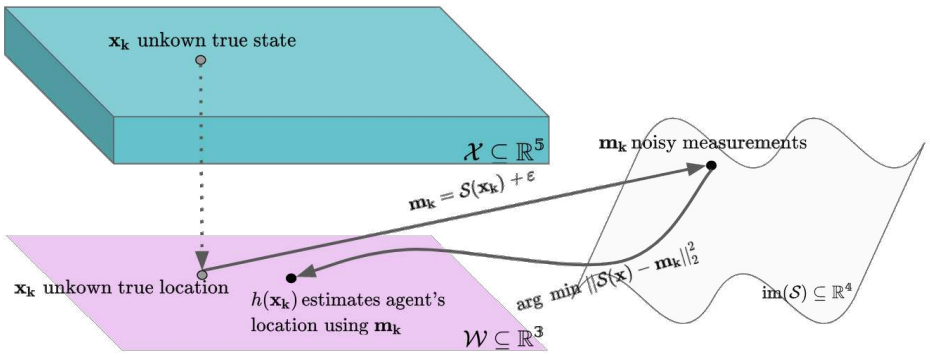

Figure 7: Underwater observation function $h(\mathbf{x}_k) = \mathbf{z_k}$ using the 3D SDUE map. Further details on the performance of (16) can be found in Fuentes et al. (2022).

5. Results

This section presents estimator outcomes based on AOI data. We analyze the data distribution, justifying EKF suitability. Demonstrations showcase EKF effectiveness in state estimation.

5.1. Predictions

Table 3
In-situ Data Collected

Type	Source	Number of Samples
Water Depth (ft)*	NOAA chart 11467	20
Surface Water Quality	YSI EXO2 Sonde	126**
Underwater Water Quality	YSI EXO2 Sonde	101**

*Values are converted to meters (m) before use.
**Unprocessed and collected across several trajectories, carried out on October 7th, 2022.

Table 4
Colocated Data

Type	Count[1]	Min	Max	Mean	Negative[2]	Satellite
Water Depth (m)	20	2.13	4.88	3.43	0	S2
Dissolved Oxygen (mg/L)	125	0.64	6.7	4.81	0	S2
Chlorophyll-a (ug/L)	125	0.87	36.67	3.49	0	S2
Temperature (°C)	125	27.45	28.69	27.97	0	L8-9
Turbidity (FNU)	125	-0.32	1942.9	62.93	56	S2

[1]Each pixel may be colocated with 1 or more in-situ samples.
[2]Number of negative in-situ data values.

The summarized data on the total number of collected water quality samples is detailed in Table 3. Additionally, Table 4 outlines the number of in-situ samples coinciding with remote sensing data from uncontaminated water, including basic statistical analyses for various water quality parameters.

Linear regression estimators, predicting surface water estimates based on co-located surface data, are illustrated in Figure 8. Similarly, KNN regressor estimators, formulated for predicting underwater estimates using corresponding underwater data, are displayed in Figure 9.

With remarkable consistency across varying maximum water depths, trends for each water quality parameter are consistent, except for DO, which exhibits noticeable divergence. The observed noise towards the end of the data series

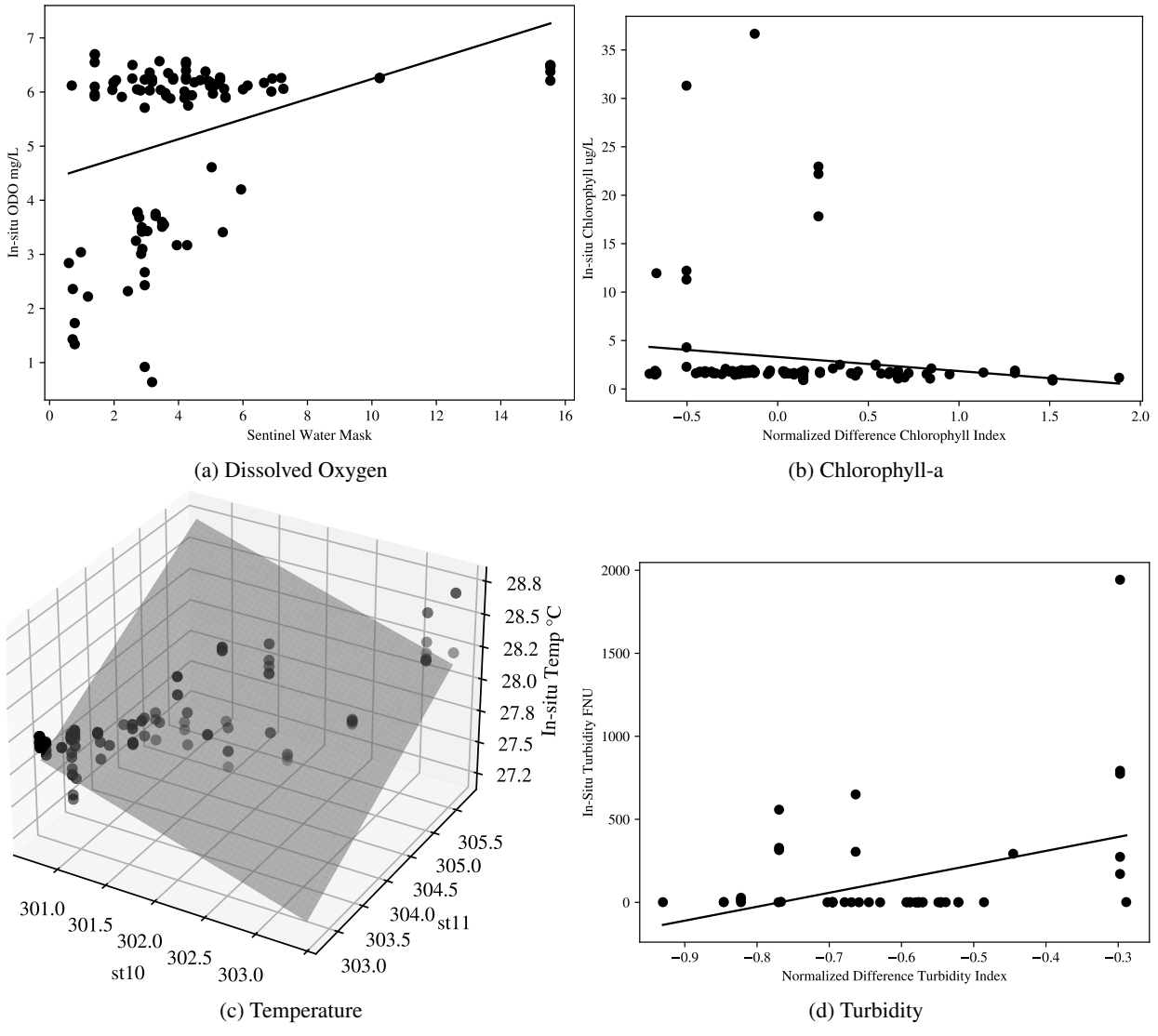

(a) Dissolved Oxygen

(b) Chlorophyll-a

(c) Temperature

(d) Turbidity

Figure 8: Linear regression estimators where remote sensing data (SWM, NDCI, ST10, ST11, NDTI) is labeled with in-situ data (DO, Chlorophyll-a, Temperature, Turbidity). Temperature is a 2D linear regression because L8-9 has two thermal infrared sensors, ST10 and ST11.

is likely due to the EXO2 sonde transitioning from initial surface measurements to deeper water as it was lowered to the ocean floor, potentially interacting with objects on the seabed.

The results presented utilized L8-9 and S2 imagery captured on October 22nd, 2022, and October 23rd, 2022, respectively, as shown in Figure 10a and Figure 10b, serving as input for the surface-level estimators. Figure 11a provides a top-level view of the predicted bathymetry, where land pixels default to 0, and water pixels predicted to have negative water depth are adjusted to a depth of one. Most water pixels with outlier estimates are located outside the main water body, within $\mathcal{P}$, or close to non-water pixels. Figure 11b visualizes the deepest predicted depths, represented in green, with most water pixels predicted to be over two meters deep, and pixels closer to the land more likely to have a predicted depth of under two meters.

Figure 12 displays the predicted sea surface water quality parameter estimates, with a few negative outliers that need to be removed. Figure 13 illustrates the predicted water quality parameter estimates for the first four layers of the SDUE for each parameter, with the negative outliers removed. Temperature estimates in the top-right section of the

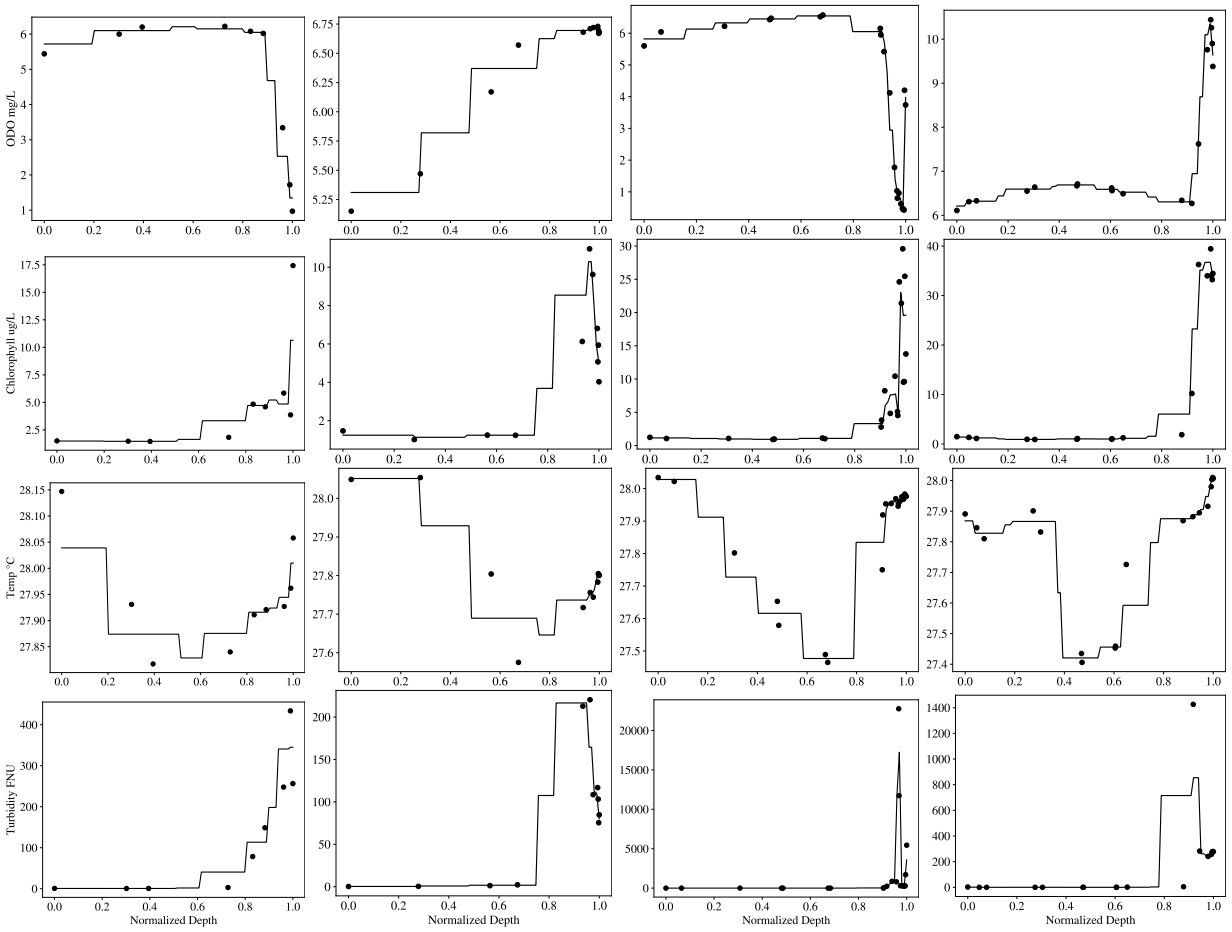

(a) Drop Location 1 (b) Drop Location 2 (c) Drop Location 3 (d) Drop Location 4

Figure 9: KNN Regressor estimators created using in-situ data collected by dropping a sensor from the water surface and lowering it to the bottom at 4 different drop sites. Depth has been normalized to a number between 0 and 1. (row 1) Dissolved Oxygen. (row 2) Chlorophyll-a. (row 3) Temperature. (row 4) Turbidity.

AOI are unavailable due to cloud coverage. Higher DO, chlorophyll, and turbidity concentrations appear in the lower depths of each pixel. For temperature estimates, the surface estimate initially cools before warming up again.

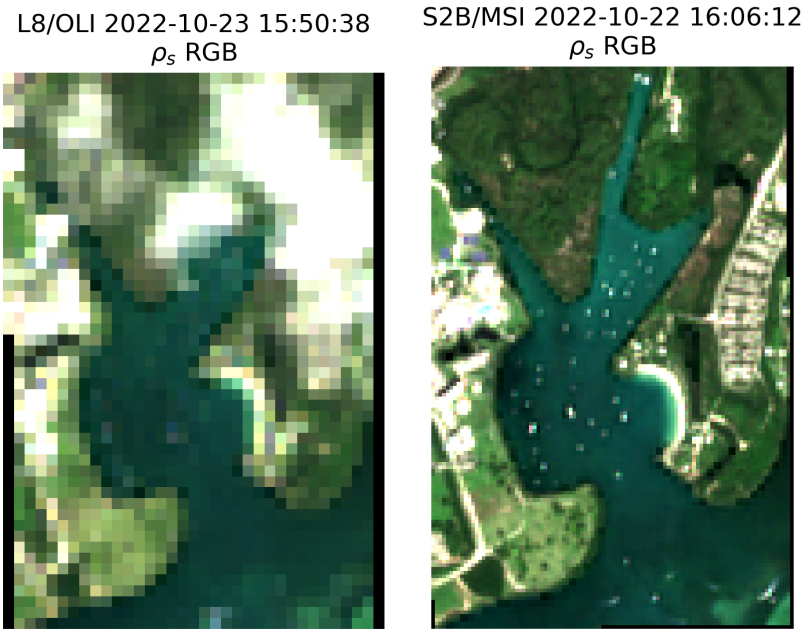

(a) ACOLITE processed Landsat 8 image (b) ACOLITE processed Sentinel 2 image

Figure 10: Images used as input for the water quality parameter estimation.

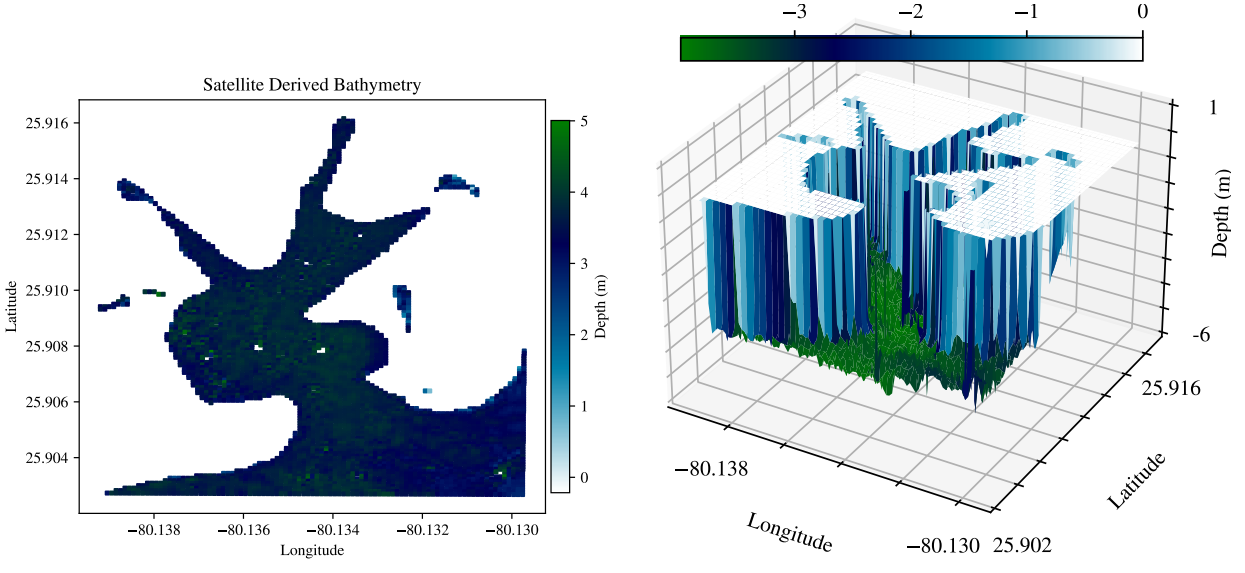

(a) 2D top-level view. (b) 3D surface view.

Figure 11: Satellite Derived Bathymetry

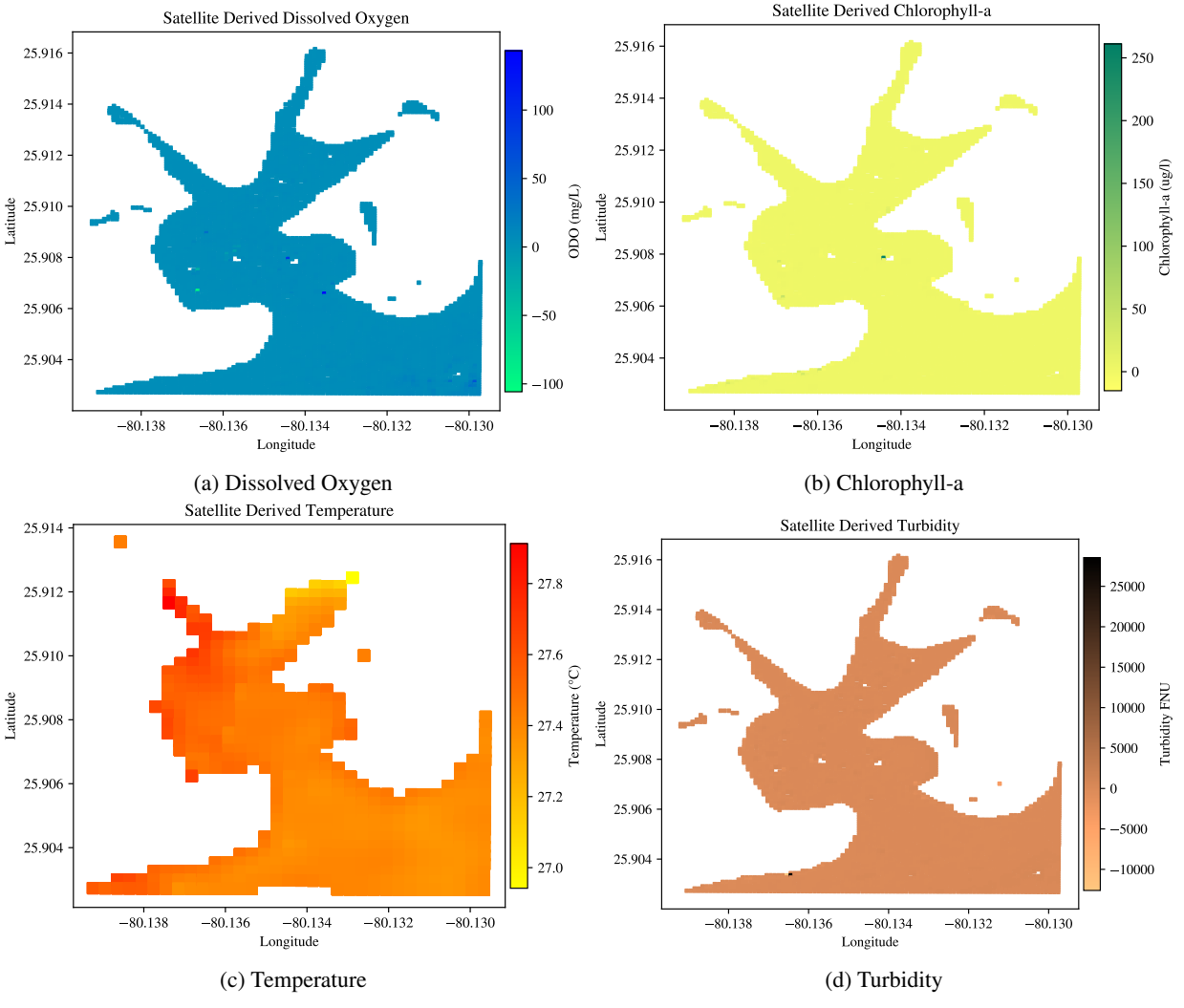

(a) Dissolved Oxygen

(b) Chlorophyll-a

(c) Temperature

(d) Turbidity

Figure 12: Satellite-derived water quality parameters with outliers.

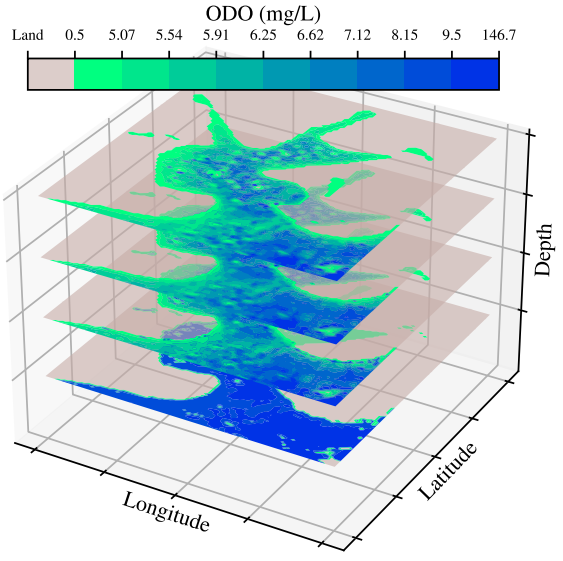

(a) 3D Satellite-Derived Dissolved Oxygen

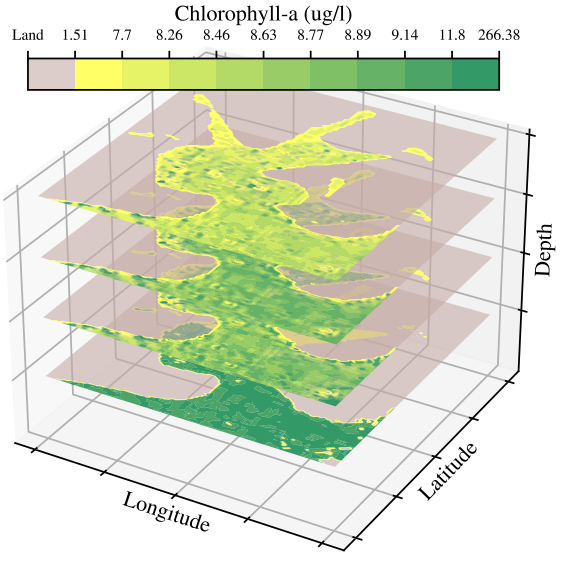

(b) 3D Satellite-Derived Chlorophyll-a

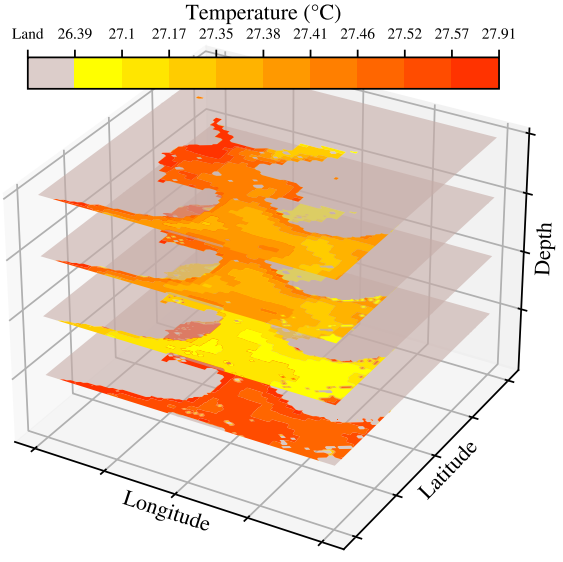

(c) 3D Satellite-Derived Temperature

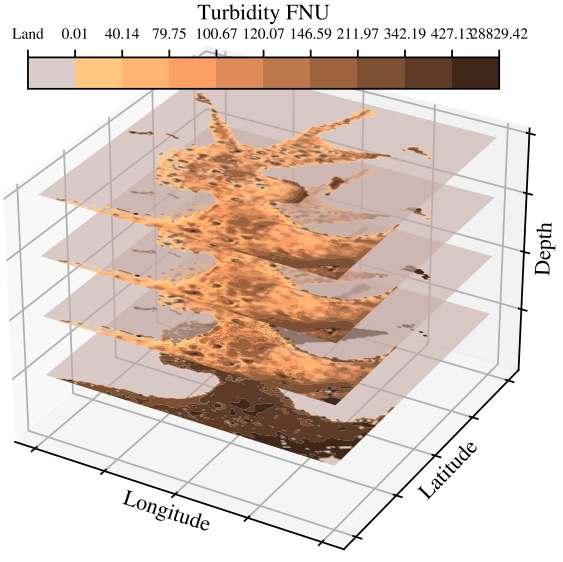

(d) 3D Satellite-Derived Turbidity

Figure 13: Satellite-derived water quality parameters extended to lower depths using the nearest KNN regressor estimator available and negative outliers replaced with a predetermined minimum value.

5.2. Data distribution

The Kalman Filter and its extension, the EKF, assume that the data originates from a normal distribution. To validate this assumption, we analyzed the data behavior post-application of Machine Learning estimators for predicting water quality features across various depth levels in our AOI. Q-Q plots for each water feature were generated, and the results are presented in Figures 14 and 15.

Most of the data generally adheres to a normal distribution or a multimodal normal distribution, with a few outliers. This suggests that atypical measurements are more prevalent than expected under a normal distribution. However, the prevalence of normal-shaped distributions (or multimodal normal-shaped distributions) indicates their suitability as models to describe the overall behavior of our data. Moreover, this justifies EKF as a suitable model to fuse the data during the state estimation task.

5.3. Path Tracking Simulation

The experimental setup for our underwater vehicle state estimation system simulation involved using ground truth for comparison purposes while control inputs, such as a steady forward speed and sinusoidal depth or yaw variations, drove the UUV. The simulation incorporated different sensor errors through actuator noise and sensor noise parameters, with the actuator noise modeled for velocity, vertical speed, and yaw rate, and sensor noise for water quality measurements. The state covariance matrix accounted for uncertainties in position, yaw angle, and velocity, while the observation covariance matrix varied with depth to reflect increased uncertainty. Simulation parameters are based on the discussion presented in Section 4.4.

We present two vehicle trajectories within the framework depicted in Figure 6. For our simulations, we consider the GPS signal becoming unavailable when the vehicle descends below 30 cm from the water surface.

The first trajectory, shown in Figure 16(a), maintains a constant heading angle, with the vehicle moving at a steady forward speed ($v = 2m/s$). The depth control input u_l follows a sinusoidal pattern, defined as $u_l = -0.1\sin(0.05t)$.

The second trajectory, illustrated in Figure 16(b), involves the vehicle moving at a constant forward speed on the surface ($v = 2.5m/s$) for half of the simulation time. Subsequently, it submerges in a sinusoidal descent for the remaining simulation, reaching a depth of 5 meters. The angular velocity behavior is defined by $\omega = 0.05\cos(0.002\pi t)$.

Our simulations comprised three phases. In the initial phase, we employed the trajectory from Figure 16(a) and utilized the SDUE as an additional sensor. Focusing on individual water parameters (DO, chlorophyll-a, temperature, turbidity), Figure 17 indicates that SDUE maps from DO and temperature data exhibited slightly lower estimation errors than those based on chlorophyll-a and turbidity.

The second phase involved experiments with the trajectory from Figure 16(b) and 3D SDUE maps based on combined water parameters. Three maps were created: one combining chlorophyll-a and DO, another combining chlorophyll-a, DO, and turbidity, and a third combining chlorophyll-a, DO, turbidity, and temperature. Figure 18 reveals that the SDUE map based on the four water parameters provided better x-coordinate estimations and comparable results compared to the other combined maps.

In the final phase, we compared dead-reckoning and EKF-based estimations for different trajectories using the full SDUE map. The results in Figure 19 align with expectations, showcasing that the EKF-based approach minimizes tracking errors at the surface and underwater compared to dead-reckoning.

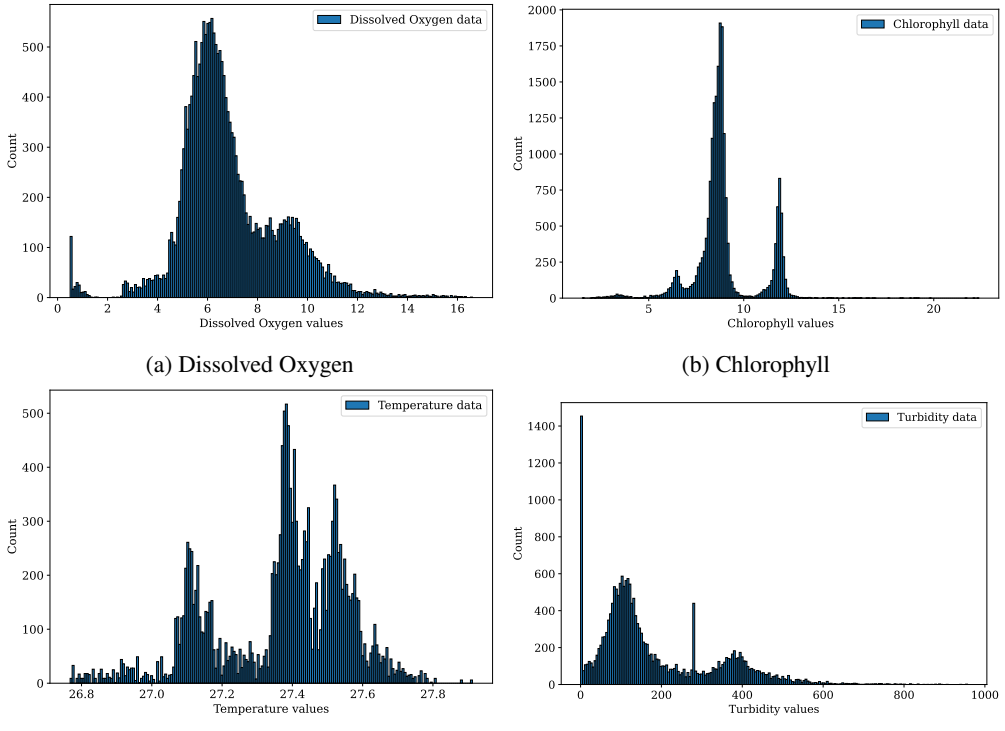

(a) Dissolved Oxygen

(b) Chlorophyll

(c) Temperature

(d) Turbidity

Figure 14: Water quality histograms (rounded to 3 standard deviations). They show the distributions are normal-shaped or multimodal normal-shaped.

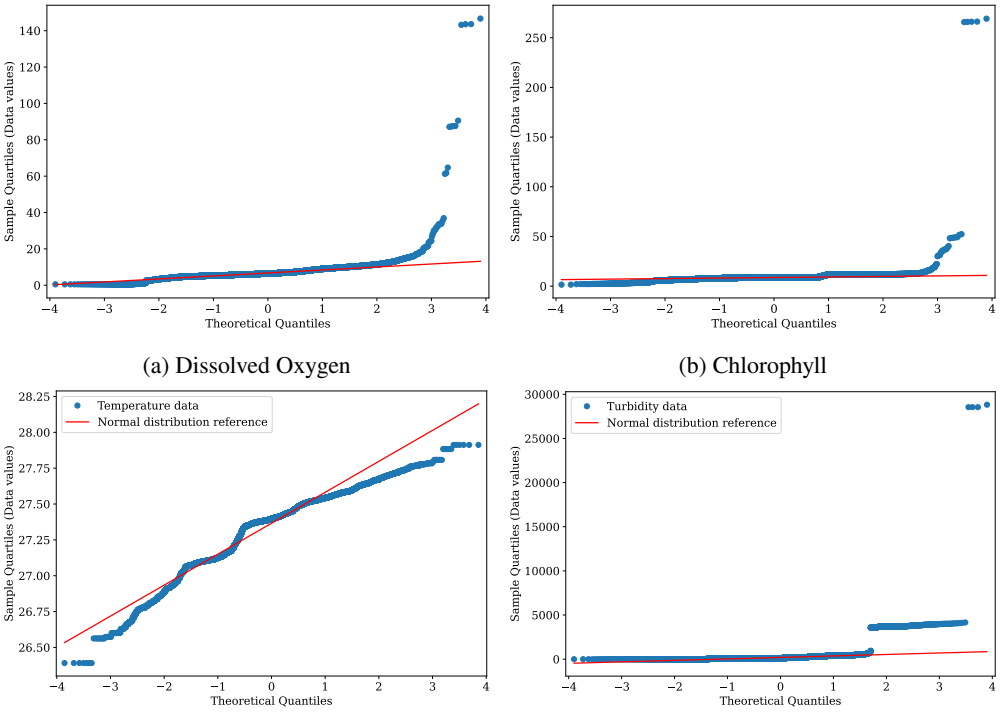

(a) Dissolved Oxygen

(b) Chlorophyll

(c) Temperature

(d) Turbidity

Figure 15: Q-Q plots for each water feature against a normal distribution. The more the data follow the line, the more normally distributed the data are.

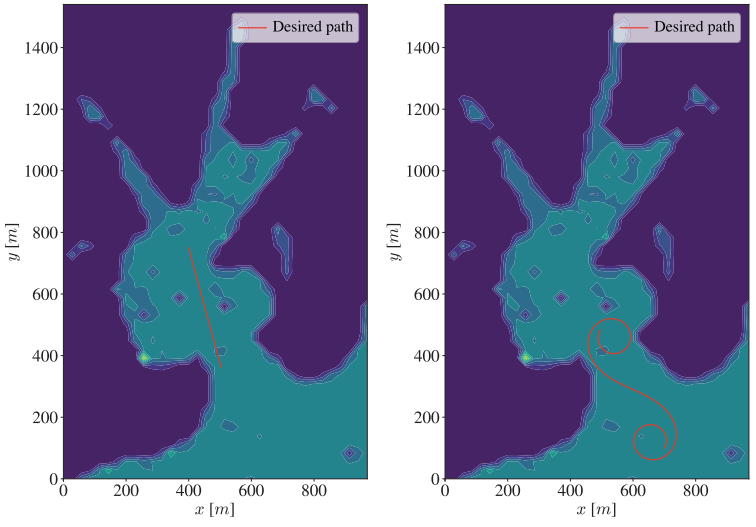

(a) Desired sinusoidal depth path

(b) Desired yaw path

Figure 16: Experimental trajectories within the SDUE

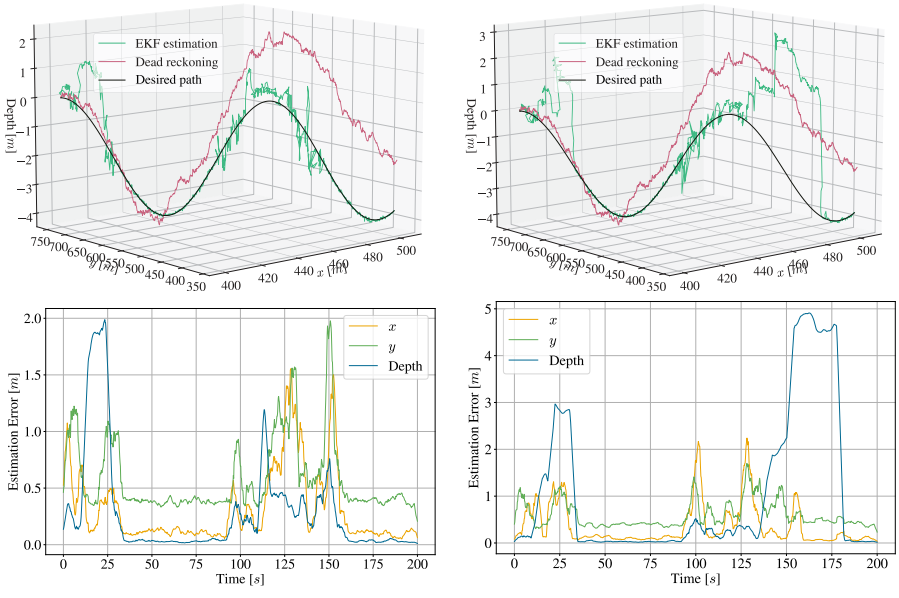

(a) Dissolved Oxygen (b) Chlorophyll

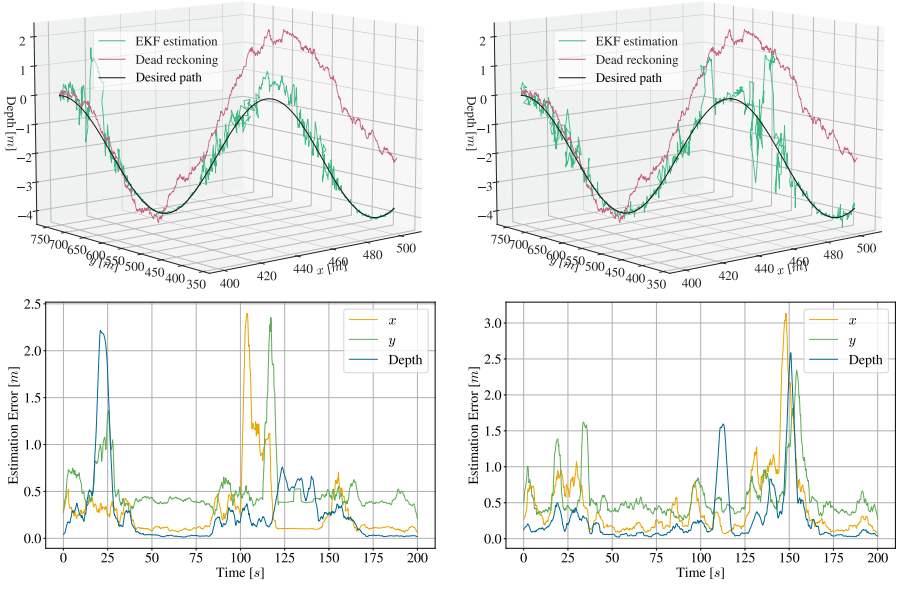

(c) Temperature (d) Turbidity

Figure 17: Dead reckoning, EKF-based estimation, and estimation errors using a single water feature from the SDUE for the first trajectory (Figure 16(a))

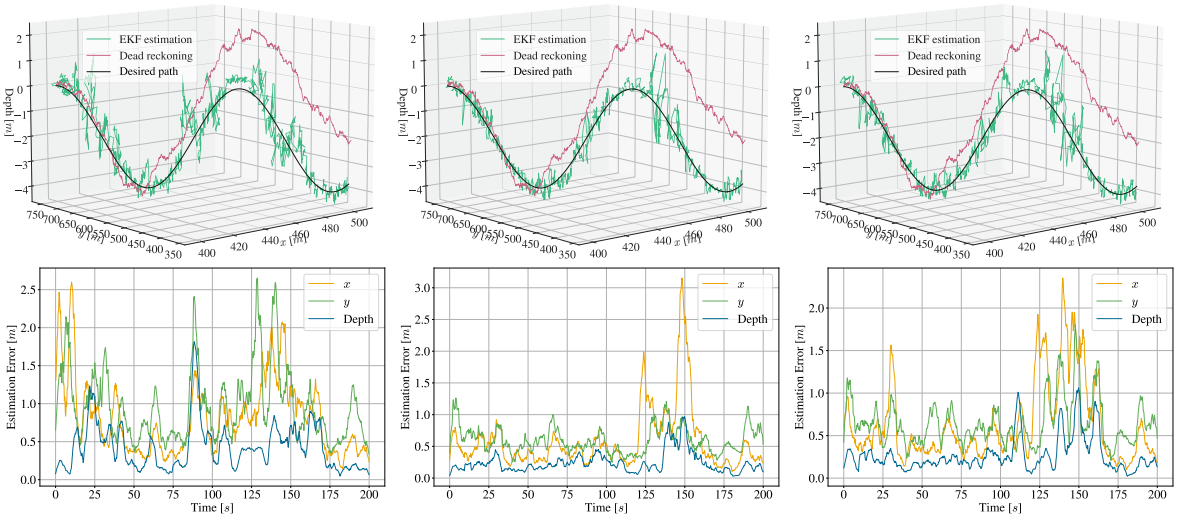

(a) Chlorophyll-a and Dissolved Oxygen

(b) Chlorophyll-a, Dissolved Oxygen and Turbidity

(c) Chlorophyll-a, Dissolved Oxygen, Temperature, and Turbidity (full SDUE)

Figure 18: Dead reckoning, EKF-based estimation, and estimation errors using combined water features from the SDUE for the first trajectory (Figure 16(a))

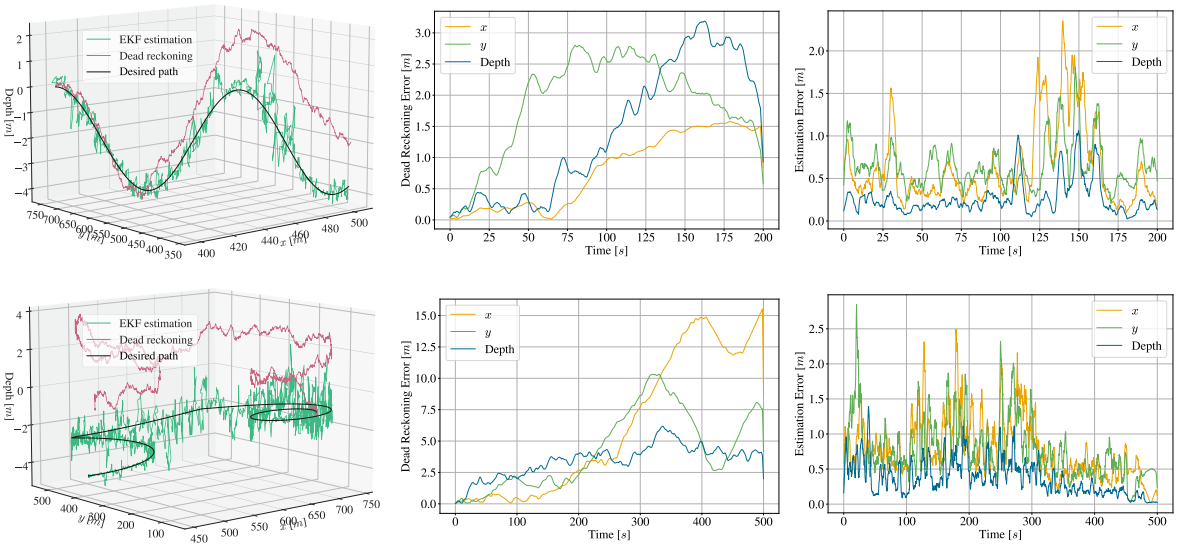

(a) Vehicle 3D paths

(b) Dead reckoning error

(c) EKF aided by the entire SDUE error

Figure 19: Comparison of dead-reckoning errors and EKF-based estimation errors using satellite-derived underwater environment maps. The first row shows the results for the first trajectory (Figure 16(a)). The second row shows the simulation results for the second trajectory (Figure 16(b)).

6. Conclusions

This paper introduces a robust approach for integrating remote-sensing and in-situ data to predict ocean models, utilizing data from S2 and L8-9 satellites. By leveraging previously studied proven methods, we predict key sea surface water quality parameters and extend them to lower depths. These predictions include bathymetry, chlorophyll-a, dissolved oxygen, turbidity, and sea surface temperature. The methodology significantly enhances the state estimation capabilities of underwater vehicles.

In the context of robot state estimation, we employ supervised machine learning estimators with an EKF solution. Computer simulations validate the practicality and effectiveness of our approach, demonstrating the accuracy of EKF with our estimations. Notably, our water depth predictions, informed by in-situ data, reveal a downward trend with increasing proximity of a water pixel to a land pixel. The selected water detection techniques prove effective even under dynamic conditions, such as cloud obstructions. Integrating applications from a second satellite further enhances estimator performance within the EKF framework.

Our comprehensive data plan, encompassing data management, collection, processing, colocation, and application development, streamlines research processes and enhances reproducibility. Organized file hierarchy, consistent naming conventions, and automation scripts contribute to ease of replication and accessibility. These systematic practices extend the research's potential impact on water quality monitoring and disaster response strategies, emphasizing our commitment to environmental management.

However, it is crucial to acknowledge limitations highlighted in the introduction. While innovative and effective, our approach relies on selected methods that may not be universally optimal for all marine environments. Case-specific evaluations are essential. The complexities of dynamic underwater environments may pose challenges not fully addressed by our methods. Despite these limitations, our research presents promising advancements in underwater state estimation and environmental management.

7. Future Work

This work lays the groundwork for a comprehensive integration of remote-sensing and in-situ data for predicting water quality parameters. However, there are avenues for substantial improvement and expansion of the capabilities of the SDUE through further research and development.

An immediate focus for improvement involves automating remaining manual steps in the methodology to streamline the process, reduce potential errors, and enhance reproducibility.

To enhance prediction accuracy and resolution, gathering additional in-situ samples from deeper waters within $\mathcal{W}$ is recommended. A more diverse and extensive dataset would improve predictions and potentially reveal novel patterns. Obtaining more underwater samples would allow the use of more advanced machine learning estimators and validation of NOAA chart 11467 data.

Incorporating higher-resolution hyperspectral data could provide more specific predictions by leveraging unique spectral signatures. Recent advancements in spectral unmixing techniques could be explored for real-time insights. An improvement strategy involves updating the SDUE during deployment as the UUV or nearby agents gather data, following a methodology similar to Kodgule et al. (2019).

In the long term, integrating higher-frequency remote data sources such as Sentinel-3 or Planet Labs could provide more up-to-date information, improving the methodology's practical utility.

From a machine learning perspective, exploring alternative estimators like Support Vector Machines and different filtering methods such as unscented Kalman filters or particle filters may enhance prediction accuracy.

Adjustments to the indices and masks used and incorporating additional water quality parameters for estimate correction could optimize data processing. Integrating other parameters like water current may lead to more holistic predictions. Additionally, we aim to ensure the robustness of our state estimation technique under various motion patterns. To this end, we plan to include other motion patterns, such as straight-line trajectory, to assess their impact on state estimation accuracy. This will provide a more comprehensive evaluation of our system.

Beyond these improvements, combining the SDUE with intelligent sampling approaches for predicting aquatic phenomena could enable proactive and responsive water quality monitoring strategies Manjanna, Quattrini Li, Smith, Rekleitis and Dudek (2018). Besides that, we could further investigate the use of the proposed SDUE as a complementary technique for state-estimation methods in modern underwater navigation planners Xanthidis, Kelasidi and Alexis (2023).

Pursuing these future directions will contribute to advancing remote-sensing and in-situ data integration, aligning with the goal of preserving water bodies.

8. Declaration of competing interest

The authors declare that they have no known competing financial interests or personal relationships that could have appeared to influence the work reported in this paper.

9. Data Availability

The data that supports the findings of this study and the accompanying source code are openly available in our public repository at https://github.com/cesarandresrojas/combining_remote_and_in-situ_sensing_journal_2023. Further instructions to facilitate reproducibility are also provided at this repository.

10. Acknowledgment

This work is supported in part by National Science Foundation grants IIS-2034123, IIS-2024733, IIS-2331908, the Office of Naval Research grant N00014-23-1-2789, the DoD grant 78170-RT-REP, and by the U.S. Dept. of Homeland Security grants 2017-ST-062000002 and 23STSLA00016-01-00.

This material is based upon work supported by the National Science Foundation under Grant No. HRD-1547798 and Grant No. HRD-2111661. These NSF Grants were awarded to Florida International University as part of the Centers of Research Excellence in Science and Technology (CREST) Program.

The work is also supported by scholarships from the National Aeronautics and Space Administration (NASA), the National GEM Consortium, and the ESA Network of Resources Initiative.

We would also like to extend our gratitude to the following personnel from Florida International University who facilitated our data collection efforts: Anthony Devesa, Miguel Cabrera, Heidys Cabrera, Luana Okino Sawada, Camilo Roa, and William H. Chamberlain.

This is contribution number 1614 from the Institute of Environment, a Preeminent Program at Florida International University.

Appendices

A. Supplementary Information

Table 5
Spectral bands for Landsat 8 and 9 sensors. Adapted from official specifications provided by USGS.

Band	Description	Wavelength range (nm)	Spatial resolution (m)
1	Coastal Aerosol	430 - 450	30
2	Blue	450 - 510	30
3	Green	530 - 590	30
4	Red	640 - 670	30
5	Near-Infrared	850 - 880	30
6	SWIR 1	1570 - 1650	30
7	SWIR 2	2110 - 2290	30
8	Panchromatic	500 - 680	15
9	Cirrus	1360 - 1380	30
10	Thermal Infrared 1 (TIRS)	10600 - 11190	100
11	Thermal Infrared 2 (TIRS)	11500 - 12510	100

Table 6
Spectral bands for the Sentinel-2 sensors (S2A & S2B). Adapted from official specifications provided by ESA.

Band	Description	S2A		S2B		Spatial resolution (m)
		Central wavelength (nm)	Bandwidth (nm)	Central wavelength (nm)	Bandwidth (nm)	
1	Coastal Aerosol	442.7	21	442.3	21	60
2	Blue	492.4	66	492.1	66	10
3	Green	559.8	36	559.0	36	10
4	Red	664.6	31	665.0	31	10
5	Vegetation red edge	704.1	15	703.8	16	20
6	Vegetation red edge	740.5	15	739.1	15	20
7	Vegetation red edge	782.8	20	779.7	20	20
8	NIR	832.8	106	833.0	106	10
8a	Narrow NIR	864.7	21	864.0	22	20
9	Water vapour	945.1	20	943.2	21	60
10	SWIR - Cirrus	1373.5	31	1376.9	30	60
11	SWIR	1613.7	91	1610.4	94	20
12	SWIR	2202.4	175	2185.7	185	20

Table 7
Metadata fields specifications. Recommendations provided by Axiom Data Science.

Project Onset	Data Collection	Project Wrap-up
Title	Spatial Bounds	Lineage Statement
Abstract	Time Period(s)	Data Consistency Report
Purpose	Data Table Attributes	Process Steps
Contacts	(e.g., column headers)	Completeness Report
Category and Form		Status and Maintenance
Keywords		Constraints
Taxonomic Information		Metadata Info

Table 8
Predetermined water quality typical and extreme ranges

Parameter	Typical Range*	Extreme Range*‘
Bathymetry (m)	2 - 5	1 - 8
Dissolved Oxygen (mg/L)	2 - 8	0.50 - 15
Chlorophyll-a (ug/L)	0.05 - 12	0.01 - 62
Temperature (°C)	26 - 29	16 - 35
Turbidity (FNU)	1 - 500	0.01 - 1000

*The values were hand-selected and require careful consideration.

CRediT authorship contribution statement

Cesar A. Rojas: Conceptualization, Methodology, Software, Investigation, Data Curation, Writing - Original Draft, Visualization, Project administration. **Paulo Padrão:** Conceptualization, Methodology, Software, Investigation, Writing - Original Draft, Visualization. **Jose Fuentes:** Conceptualization, Methodology, Software, Formal analysis, Investigation, Writing - Original Draft, Visualization. **Gregory M. Reis:** Conceptualization, Writing - Review & Editing, Investigation, Resources. **Arif R. Albayrak:** Conceptualization, Writing - Review & Editing. **Batuhan Osmanoglu:** Conceptualization, Writing - Review & Editing. **Leonardo Bobadilla:** Conceptualization, Writing - Review & Editing, Resources, Supervision, Funding acquisition.

References

Allotta, B., Caiti, A., Costanzi, R., Fanelli, F., Fenucci, D., Meli, E., Ridolfi, A., 2016. A new auv navigation system exploiting unscented kalman filter. Ocean Engineering 113, 121–132. URL: https://www.sciencedirect.com/science/article/pii/S0029801815007271, doi:https://doi.org/10.1016/j.oceaneng.2015.12.058.

Bayat, F., Hasanlou, M., 2016. Feasibility Study of Landsat-8 Imagery for Retrieving Sea Surface Temperature (Case Study: Persian Gulf). The International Archives of the Photogrammetry, Remote Sensing and Spatial Information Sciences XLI-B8. doi:10.5194/isprs-archives-xli-b8-1107-2016.

Caballero, I., Fernández, R., Escalante, O.M., Mamán, L., Navarro, G., 2020. New capabilities of Sentinel-2A/B satellites combined with in situ data for monitoring small harmful algal blooms in complex coastal waters. Scientific Reports 10. doi:10.1038/s41598-020-65600-1.

Caballero, I., Stumpf, R.P., 2019. Retrieval of nearshore bathymetry from sentinel-2a and 2b satellites in south florida coastal waters. Estuarine, Coastal and Shelf Science 226, 106277. URL: https://www.sciencedirect.com/science/article/pii/S0272771418309983, doi:https://doi.org/10.1016/j.ecss.2019.106277.

Caballero, I., Stumpf, R.P., Meredith, A., 2019. Preliminary assessment of turbidity and chlorophyll impact on bathymetry derived from sentinel-2A and sentinel-3A satellites in South Florida. Remote Sensing 11. doi:10.3390/rs11060645.

Cruz, R.C., Costa, P.R., Vinga, S., Krippahl, L., Lopes, M.B., 2021. A review of recent machine learning advances for forecasting harmful algal blooms and shellfish contamination. doi:10.3390/jmse9030283.

Documentation, A.D.S., 2017. URL: https://www.axiomdatascience.com/best-practices/index.html. date accessed: May 19, 2023.

Drakopoulou, P., Kapsimalis, V., Parcharidis, I., Pavlopoulos, K., 2018. Retrieval of nearshore bathymetry in the Gulf of Chania, NW Crete, Greece, from WorldWiew-2 multispectral imagery. doi:10.1117/12.2326189.

Earth Science Data Systems, N., 2016. URL: https://www.earthdata.nasa.gov/engage/open-data-services-and-software/data-information-policy/data-levels.

Fox, D., et al., 2001. Particle filters for mobile robot localization, in: Doucet, A., de Freitas, N., Gordon, N. (Eds.), Sequential Monte Carlo Methods in Practice. Springer New York, New York, NY, pp. 401–428.

Fu, J., Chen, C., Guo, B., Chu, Y., Zheng, H., 2020. A split-window method to retrieving sea surface temperature from landsat 8 thermal infrared remote sensing data in offshore waters. Estuarine, Coastal and Shelf Science 236, 106626. doi:10.1016/J.ECSS.2020.106626.

Fuentes, J., Bobadilla, L., Smith, R.N., 2022. Localization in seemingly sensory-denied environments through spatio-temporal varying fields, in: 2022 Sixth IEEE International Conference on Robotic Computing (IRC), pp. 142–147. doi:10.1109/IRC55401.2022.00032.

Gholizadeh, M.H., Melesse, A.M., Reddi, L., 2016. A comprehensive review on water quality parameters estimation using remote sensing techniques. doi:10.3390/s16081298.

Hafeez, S., Wong, M., Ho, H., Nazeer, M., Nichol, J., Abbas, S., Tang, D., Lee, K., Pun, L., 2019. Comparison of Machine Learning Algorithms for Retrieval of Water Quality Indicators in Case-II Waters: A Case Study of Hong Kong. Remote Sensing 11. doi:10.3390/rs11060617.

Hook, L.A., Santhana Vannan, S.K., Beaty, T.W., Cook, R.B., Wilson, B.E., 2010. Best Practices for Preparing Environmental Data Sets to Share and Archive 1. Bulletin of the Ecological Society of America 82.

Kavats, O., Khramov, D., Sergieieva, K., Puputti, J., Joutsenvaara, J., Kotavaara, O., 2022. Optimal Threshold Selection for Water Bodies Mapping from Sentinel-L Images Based On Sentinel-2 Water Masks, in: International Geoscience and Remote Sensing Symposium (IGARSS). doi:10.1109/IGARSS46834.2022.9883600.

Kodgule, S., Candela, A., Wettergreen, D., 2019. Non-myopic Planetary Exploration Combining in Situ and Remote Measurements, in: IEEE International Conference on Intelligent Robots and Systems, pp. 536–543. doi:10.1109/IROS40897.2019.8967769.

Lacaux, J.P., Tourre, Y.M., Vignolles, C., Ndione, J.A., Lafaye, M., 2007. Classification of ponds from high-spatial resolution remote sensing: Application to Rift Valley Fever epidemics in Senegal. Remote Sensing of Environment 106, 66–74. doi:10.1016/J.RSE.2006.07.012.

Manjanna, S., Quattrini Li, A., Smith, R., Rekleitis, I., Dudek, G., 2018. Heterogeneous multi-robot system for exploration and strategic water sampling, pp. 1–8. doi:10.1109/ICRA.2018.8460759.

Manzanilla, A., Reyes, S., Garcia, M., Mercado, D., Lozano, R., 2019. Autonomous navigation for unmanned underwater vehicles: Real-time experiments using computer vision. IEEE Robotics and Automation Letters 4, 1351–1356. doi:10.1109/LRA.2019.2895272.

Mishra, S., Mishra, D.R., 2012. Normalized difference chlorophyll index: A novel model for remote estimation of chlorophyll-a concentration in turbid productive waters. Remote Sensing of Environment 117. doi:10.1016/j.rse.2011.10.016.

Nazeer, M., Bilal, M., Alsahli, M.M., Shahzad, M.I., Waqas, A., 2017. Evaluation of empirical and machine learning algorithms for estimation of coastal water quality parameters. ISPRS International Journal of Geo-Information 6. doi:10.3390/ijgi6110360.

Osmanoglu, B., 2020. Sar data format. URL: https://blogs.nasa.gov/swesarr/2020/09/08/sar-data-format/. date accessed: May 19, 2023.

Paull, L., Saeedi, S., Seto, M., Li, H., 2014. Auv navigation and localization: A review. IEEE Journal of Oceanic Engineering 39, 131–149. doi:10.1109/JOE.2013.2278891.

Potokar, E.R., Norman, K., Mangelson, J.G., 2021. Invariant extended kalman filtering for underwater navigation. IEEE Robotics and Automation Letters 6, 5792–5799. doi:10.1109/LRA.2021.3085167.

Rojas, C.A., Padrao, P.V., Fuentes, J.E., Albayrak, A.R., Osmanoglu, B., Bobadilla, L., 2022a. Combining Remote and In-situ Sensing for Autonomous Underwater Vehicle Localization and Navigation, in: Oceans Conference Record (IEEE). doi:10.1109/OCEANS47191.2022.9977208.

Rojas, C.A., Reis, G.M., Albayrak, A.R., Osmanoglu, B., Bobadilla, L., Smith, R.N., 2022b. Combining Remote and In-situ Sensing for Persistent Monitoring of Water Quality, in: Oceans Conference Record (IEEE). doi:10.1109/OCEANSChennai45887.2022.9775339.

Salas, E.A.L., Kumaran, S.S., Partee, E.B., Willis, L.P., Mitchell, K., 2022. Potential of mapping dissolved oxygen in the Little Miami River using Sentinel-2 images and machine learning algorithms. Remote Sensing Applications: Society and Environment 26, 100759. doi:10.1016/J.RSASE.2022.100759.

Salavasidis, G., Munafò, A., McPhail, S.D., Harris, C.A., Fenucci, D., Pebody, M., Rogers, E., Phillips, A.B., 2021. Terrain-aided navigation with coarse maps—toward an arctic crossing with an auv. IEEE Journal of Oceanic Engineering 46, 1192–1212. doi:10.1109/JOE.2021.3085941.

Tomchenko, O., Khyzhniak, A., Kravtsova, O., Singh, S.K., 2022. An assessment of the aquatic environment quality of the urban water bodies using system analysis methods based on integrating remote sensing data and ground information 5, 73–98. doi:10.1016/B978-0-323-85378-1.00006-4.

Xanthidis, M., Kelasidi, E., Alexis, K., 2023. Resiplan: Closing the planning-acting loop for safe underwater navigation, in: 2023 IEEE International Conference on Robotics and Automation (ICRA), pp. 3138–3145. doi:10.1109/ICRA48891.2023.10160801.